Research on Optimal Design of Ultra-High-Speed Motors Based on Multi-Physical Field Coupling Under Mechanical Boundary Constraints

Jianguo Bu *, Weifeng Zhang *, Yan Yu *, Hailong Pang , Wei Lei

Posted Date: 25 October 2024

doi: 10.20944/preprints202410.2004.v1

Keywords: ultra-high-speed motors; multi-physical field; optimal design; NSGA-2; Kriging surrogate model; Maxpro experimental design

 doi:10.20944/preprints202410.2004.v1

Article

Research on Optimal Design of Ultra-High-Speed Motors Based on Multi-Physical Field Coupling under Mechanical Boundary Constraints

Jianguo Bu, Weifeng Zhang *,Yan Yu *, Hailong Pang and Wei Lei

Army Military Transportation College, Tianjin 300161, China

* Correspondence: cheungwaiphen@163.com (W.Z.); yuyan19841125l@163.com (Y.Y.); Tel.: +15222553900 (W.Z.); Tel:18622578316 (Y.Y.)

Abstract: With the rapid development of modern industrial technology, ultra-high-speed motors have demonstrated tremendous application potential in fields such as aerospace, high-speed machining, and micro-mechanical systems due to their high efficiency, high power density, and compact structure. However, the design of ultra-high-speed motors was confronted with numerous challenges, particularly under mechanical boundary constraints, how to balance the interactions among electromagnetic performance, thermodynamic characteristics, mechanical strength, and other multi-physical fields has become a key factor limiting performance enhancement. This study first establishes a multi-physical field coupling model for ultra-high-speed motors, comprehensively considering the mutual influences of electromagnetic fields, temperature fields, and stress fields. Through finite element analysis, precise simulations are conducted on the electromagnetic distribution, heat conduction, mechanical stress, and rotor dynamics characteristics within the motor. Based on this, the impact of various design parameters (such as rotor structure, material selection, and cooling methods) on motor performance is investigated, revealing the variation laws of motor performance under multi-physical field coupling. With mechanical boundary constraints taken into account, this paper proposes an optimization design method for high-speed motors based on a multi-physical field coupling model. Initial samples are obtained through MaxPro experimental design, and a Kriging surrogate model is used for fitting. Subsequently, the NSGA-2 algorithm is employed for optimization design. During the optimization process, RMAE and RAAE are adopted for accuracy evaluation, and the Kriging model is iteratively updated based on the evaluation results until the optimal design of the ultra-high-speed motor is completed. This optimization design method enhances the overall performance of the motor while ensuring its mechanical boundary conditions and reducing the computational load during the optimization process. Experimental results demonstrate that the proposed multi-physical field coupling optimization design method can significantly improve the efficiency and power density of ultra-high-speed motors. This study not only provides theoretical support and technical guidance for the design of ultra-high-speed motors but also offers new ideas and methods for motor research and development in related fields. In the future, more efficient and intelligent optimization design algorithms will be explored to continuously advance ultra-high-speed motor technology.

Keywords: ultra-high-speed motors; multi-physical field; optimal design;NSGA-2; Kriging surrogate model; Maxpro experimental design

1. Introduction

The rotor speed of high-speed motors is usually higher than 10000 r/min, which has the advantages of high power density, small size, fast dynamic response, direct connection with high-speed loads, and high transmission efficiency [1]. It will be widely used in aviation [2–6], automotive [7–11] and other fields.

 doi:10.20944/preprints202410.2004.v1

However, the operating characteristics of this high-speed motor are significantly different from ordinary motors. Therefore, when optimizing design, it is necessary to consider factors such as rotor strength and dynamic characteristics, increased stator iron loss and rotor eddy current loss caused by high-speed, and heat dissipation and cooling in small spaces [12]. For this reason, scholars have conducted extensive research in these areas. Professor Zhang Fengge analyzed the strength of different protective measures for the possible damage to permanent magnets caused by ultra-high altitude motors, and provided design suggestions [13,14]; Dr. Zhou Fengzheng conducted a preliminary study on the influence of stator structure on rotor eddy current losses [15]. In 2019, he analyzed the effects of rotor magnetization method and rotor support structure on cogging torque and rotor dynamics, and optimized the design of the motor rotor [16]; During Dr. Qiu Hongbo's doctoral studies, he systematically studied the structural form, permeability, and conductivity of the permanent magnet sleeve of high-speed motors on the effects of rotor surface eddy current loss and heat dissipation. He innovatively proposed a weak magnetic sleeve structure for high-speed permanent magnet motors [17–19].

Professor Fang Jiancheng analyzed the impact of stator structure size on rotor eddy current losses and provided measures to reduce rotor eddy current losses [20]; Dr. Dong Jianning from Southeast University summarized the calculation methods for the losses of various parts of high-speed motors, compared the temperature rise calculation methods, and summarized the issues of rotor strength and dynamic analysis. Finally, he pointed out the problems in the design and calculation of these aspects, and looked forward to the future development direction of high-speed motors. He believed that the optimization design technology of multi physical field coupling is a key issue that needs to be studied in the future [21].

Recently, the multi physics coupling optimization design of motors has become a research hotspot. In 2019, Professor Xu Jinquan's team from Beijing University of Aeronautics and Astronautics proposed a multi physical field comprehensive design method for the hub motor of electric armored vehicles. The multi physical field coupling was decomposed into two coupled models, and then design verification was conducted separately to obtain the design results [22]; Fengge Zhang from Shenyang University of Technology established electromagnetic field, mechanical field, and temperature field models for high-speed motors, and conducted simple unidirectional coupling, based on which motor design was carried out [23]; Professor Han Bangcheng took the minimum rotor loss as the optimization objective, and the geometric size of the motor as the design variable. During the optimization process, the influence of size changes on the rotor mode and strength of the motor was considered. The NLPQL algorithm was used to complete the optimization design of a high-speed maglev permanent magnet motor, with size, electromagnetic performance, mechanical performance, and other constraints [24]; Kun Wang from Beijing University of Aeronautics and Astronautics proposed a global design method for multi physical field coupling motors and developed a flexible rotor motor supported by active magnetic bearings [25]; Jung Y H propose a design method that considers the irreversible demagnetization and mechanical characteristics at all design steps using the FEA [26]; Koronides A proposed an innovative weak coupling design procedure considering the interdependence of the phenomena involved during both preliminary and final design stages foreseen [27]; Gu Y presents a mechanical multi-objective optimal design of HSPMSM based on parametric sensitivity analysis [28]; Kim J H proposed design process enables ultra-high-speed motor design while considering mechanical stresses of the rotor materials according to the temperature [29]; In order to reduce the computational burden during the optimization design process, researchers propose using a surrogate model to represent the finite element model [30,31].

It can be seen that how to improve the accuracy and calculation speed of the multi physical field coupling model for ultra high speed motors, and achieve global optimization design, is a problem that needs to be solved in current research and has become a hot research topic.

2. Motor Topology

 doi:10.20944/preprints202410.2004.v1

Ultra high speed motors consider reducing the frequency of magnetic field alternating and causing an increase in iron loss. Generally, 1 or 2 pairs of permanent magnets are used, and for internal rotor motors, carbon fiber sleeves need to be designed. The topology structure of the motor studied in this article is shown in Figure 1, which adopts a 1-pair pole, inner rotor, 18 slots, and distributed winding structure.

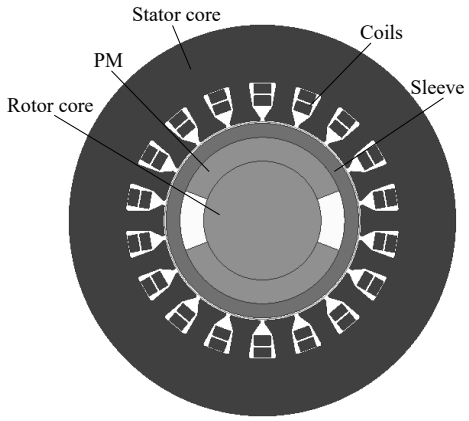

Figure 1. Motor topology.

The specific design indicators are shown in Table 1, and the initial design parameters are shown in Table 2.

Table 1. Design indicators.

Parameters	Value
Rated line voltage (V)	380
Rated power (kW)	12
Rated speed (r/min)	100000
Rated Efficiency(%)	>95

Table 2. Design indicators.

Parameters	Value(mm)
Outer diameter of stator (D_{o1})	110
Outer diameter of rotor core (D)	40
Armature length (L_{ef})	48
Thickness of permanent magnet (h_{Nd})	2
sleeve thickness (h_{Sleeve})	2
Air gap length (L_{Airgap})	0.8

3. Mechanical Modeling and Analysis of Motor Rotors

3.1. Rotor Dynamics Model

The simplified rotor-bearing system mainly includes shaft segments, rigid discs, and bearings, as shown in Figure 2.

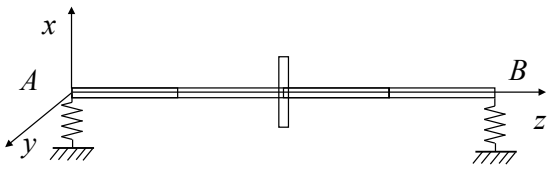

Figure 2. Typical dynamic model of rotor bearing system.

 doi:10.20944/preprints202410.2004.v1

The rotor motion equation can be expressed as:

$$\boldsymbol{M\ddot{u} + G\dot{u} + Ku = Q} \quad (1)$$

where, $\boldsymbol{M}$ is mass matrix, $\boldsymbol{G}$ is gyroscopic matrix, $\boldsymbol{K}$ is stiffness matrix, $\boldsymbol{u}$ is generalized coordinate, $\boldsymbol{Q}$ is generalized force. $\boldsymbol{M}$ and $\boldsymbol{K}$ are real symmetric positive definite matrices, and $\boldsymbol{G}$ is real anti symmetric matrix. The critical angular velocity of synchronous forward vortex can be obtained by solving the frequency equation.

3.2. Calculation of Critical Speed and Vibration Mode of a Single Rotor

According to Table 3, the preliminary rotor parameters are given. At this time, the rotor length is 288.5mm, the mass is 1.685kg, the thickness of the permanent magnet is 1mm, and the thickness of the sleeve is 1mm. Set the bearing stiffness to 1×10^6N/m, The imbalance level to G2.5 (100,000 rpm), and the rotor imbalance to 0.4 gmm. The imbalance force is evenly distributed on the two impellers, with an angle of 90° for the imbalance amount.

Table 3. Rotor Parameters.

First layer (steel)		Second layer (PM)		Third layer (carbon fiber)		*L*/mm	Number of segments	notes
D_1/mm	ϱ_1/ kg/m^3	D_2/mm	ϱ_2/ kg/m^3	D_3/mm	ϱ_3/ kg/m^3			
12	7850	12	0	12	0	18	1	
40	7850	40	0	40	0	26	2	Impeller position
20	7850	20	0	20	0	21	1	
24	7850	24	0	24	0	30	2	bearing position
24	7850	24	0	24	0	20	1	
38	7850	38	0	38	0	9.1	1	
38	7850	40	8400	42	1600	56.3	3	Magnetic pole position
38	7850	38	0	38	0	9.1	1	
24	7850	24	0	24	0	9	1	
24	7850	24	0	24	0	30	2	bearing position
20	7850	20	0	20	0	16	1	
40	7850	40	0	40	0	26	2	Impeller position
12	7850	12	0	12	0	18	1	

Figure 3a shows the Campbell diagram of the rotor, and the critical speed of the system can be obtained by the intersection of the natural frequency and synchronization curve at different rotational speeds in this diagram. Within the given speed range, it can be observed that the rotor has experienced a total of 6 critical speeds, corresponding to 3 critical speeds of reverse precession and 3 critical speeds of forward precession. Due to the difficulty in excitation of the critical speed of anti precession, only the first three orders of forward precession critical speed of the rotor were extracted. The first three critical speeds for forward propulsion of the rotor system are 9378rpm, 10390rpm, and 102385rpm, respectively.

Figure 3b shows the vibration modes corresponding to the first three critical speeds of the rotor. The first mode is conical, the second mode is cylindrical, and the third mode is curved. This indicates that the first two modes are rigid modes, in which the critical speed is caused by the low stiffness of the bearing, and the rotor can be considered as a rigid body. The third mode is a bending mode, in which the critical speed is caused by the bending of the rotor, and the rotor can be considered as a flexible rotor. Due to the low speed of the rigid mode, the bending mode is generally the focus of investigation.

 doi:10.20944/preprints202410.2004.v1

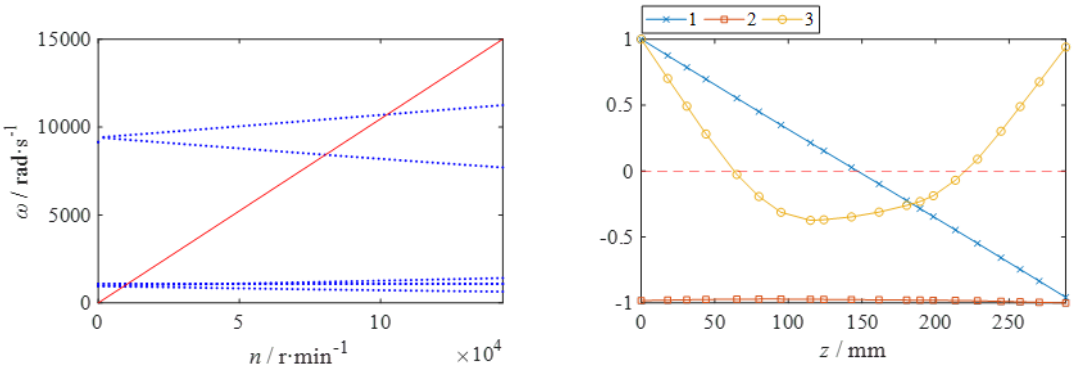

(a) (b)

Figure 3. Analysis of critical speed and vibration mode of rotor. (a) Campbell diagram;(b) Rotor vibration mode diagram.

Due to the bending critical speed of the rotor being 102385 rpm, which is very close to the rated speed of the motor, the amplitude of vibration of the motor at rated speed is very large. It is necessary to change the rotor parameters to increase the critical speed of the rotor. Generally, the measures to increase the bending critical speed of the rotor include increasing the diameter of the rotor and reducing the length of the rotor. The following discusses the relationship between increasing the diameter of each part and reducing the length and critical speed.

Figure 4a shows the effect of the diameter of the bearing section on the critical speed. It can be seen from the figure that the diameter of this section has little effect on the first to second order critical speeds. As the diameter increases, the third order critical speed increases significantly. When the diameter reaches 30mm, the critical speed exceeds 140,000rpm, with a high stability margin. Therefore, it is appropriate to use a diameter of 30mm for this section.

Figure 4b shows the effect of the armature length on the critical speed. It can be seen from the figure that this parameter has little effect on the first and second order critical speeds. As the length increases, the third order critical speed decreases due to the increase in rotor length directly increasing the length of the rotor, thereby reducing the critical speed. Within the allowable range of electromagnetic force, this distance should be shortened as much as possible. Considering the balance of electromagnetic force and critical speed, a length of between 40mm and 56 mm is appropriate.

Figure 4c shows the effect of the outer diameter (D) of the rotor iron core on the critical speed. It can be seen from the figure that this diameter has little effect on the first and second order critical speeds. As the inner diameter increases, the third order critical speed increases. When the diameter is greater than 38mm, the increase in critical speed slows down. Therefore, D is selected to be no less than 38mm.

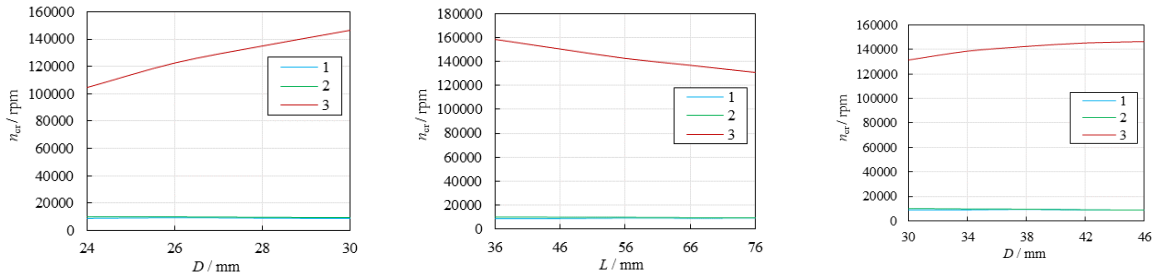

(a) (b) (c)

Figure 4. Bending patterns of the rotor at different rotational speeds: (a) Diameter of bearing section; (b) Length of permanent magnet; (c) Outer diameter of rotor core.

 doi:10.20944/preprints202410.2004.v1

Based on rotor dynamic optimization results, further optimization of motor electromagnetic performance can require an armature length (L_{ef}) of ≤56mm and a rotor iron core outer diameter(D) of ≥38mm.

3.3. Rotor Strength Analysis

Due to material characteristics of permanent magnets, they can withstand large compressive stresses but cannot withstand large tensile stresses. Therefore, a protective sleeve is usually added around the permanent magnet to provide a radial preload between the sleeve and permanent magnet to compensate for tensile stresses generated by centrifugal forces during high-speed rotation.

The calculation method for tensile stress and compressive stress in permanent magnets can be analyzed through elastic mechanics theory or calculated using finite element software. Since there is little deviation between theoretical solutions and finite element solutions, simplified calculations are used in this paper for analysis.

Firstly, we analyzed the influence of D on stress distribution in permanent magnets. By rotor dynamic analysis, it can be known that when D≥38mm, take an inner diameter range of 38~50mm. At this time, take permanent magnet thickness as 1mm, h_{Sleeve}as 2mm, and interference fit between permanent magnet and protective sleeve as 0.1mm. The stress distribution includes static stress distribution after assembly and stress distribution during rotation considering the limit condition of motor overspeed operation at $n = 120000rpm$.

Figure 5a shows radial stress distribution in permanent magnets under static state, where stress symbols with negative values represent compressive stress. It can be seen that compressive stress gradually increases from inside to outside along the direction of permanent magnet thickness. As the shaft diameter increases, compressive stress decreases. Figure 5b shows tangential stress distribution in permanent magnets under static state, where stress slightly decreases from inside diameter to outside diameter along the direction of permanent magnet thickness. As the shaft diameter increases, compressive stress decreases.

Figure 5c shows radial stress distribution in permanent magnets under dynamic state, where radial pressure is slightly higher than static pressure. Figure 5d shows tangential stress distribution in permanent magnets under dynamic state, where tangential pressure is significantly lower than static pressure and decreases more obviously with increasing D, which may be related to higher centrifugal force influence with larger D.

Typically, permanent magnets can withstand a maximum compressive stress limit of about 1000MPa and a maximum tensile stress limit of about 80MPa. Therefore, under these conditions, when D is within the range of 38~50mm, stress distribution meets strength requirements.

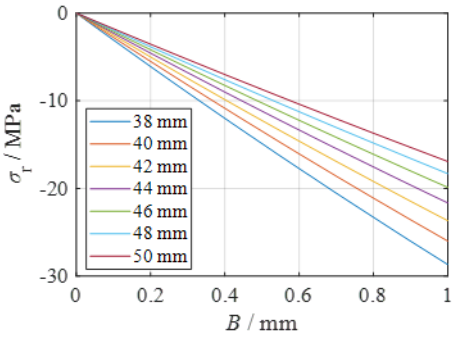

(a)

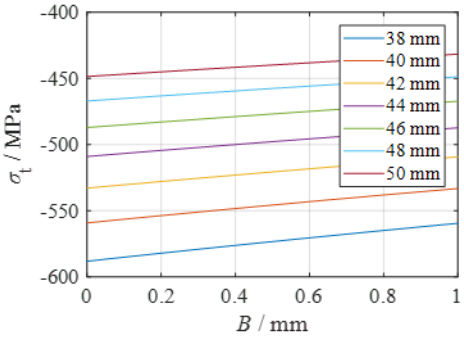

(b)

Preprints.org (www.preprints.org) | NOT PEER-REVIEWED | Posted: 25 October 2024 doi:10.20944/preprints202410.2004.v1

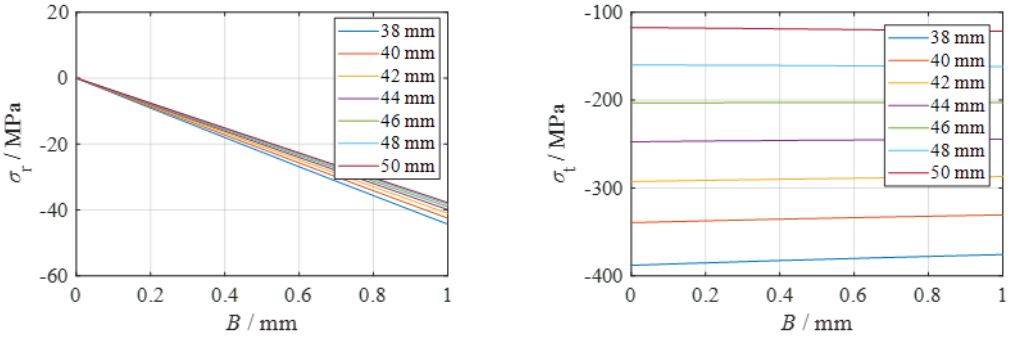

(c) (d)

Figure 5. Stress distribution along the thickness direction of permanent magnets under different rotor core outer diameter conditions: (a) Static radial stress; (b) Static tangential stress;(c) Dynamic radial stress;(d) Dynamic tangential stress.

Taking D as 40mm and other conditions unchanged, analyze the influence of h_{Nd} on stress. The range of h_{Nd} is 1-4mm.

Figure 6a shows the radial stress distribution of permanent magnet in static state. With the increase of h_{Nd}, the radial compressive stress decreases. Figure 6b shows the tangential stress distribution of permanent magnet in static state. With the increase of h_{Nd}, the tangential compressive stress decreases.

Figure 6c shows the radial stress distribution of permanent magnet in dynamic state, and the radial pressure is somewhat higher than that in static state. Figure 6d shows the tangential stress distribution of permanent magnet in dynamic state, and the tangential pressure is significantly lower than that in static state. With the increase of h_{Nd}, the compressive stress gradually becomes tensile stress. When h_{Nd} is greater than or equal to 3.5mm, the tensile stress exceeds the tensile limit and the permanent magnet is damaged.

It can be seen that the increase of h_{Nd} will cause the tensile stress of permanent magnet to exceed the tensile limit and should be limited.

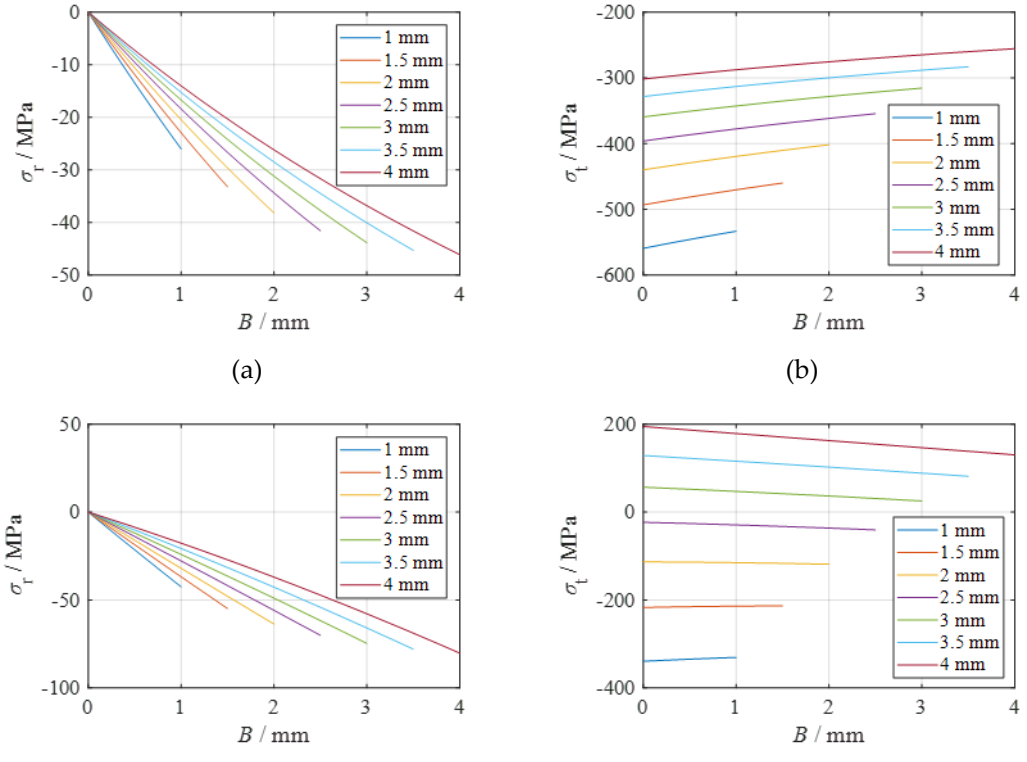

(a) (b)

(c) (d)

 doi:10.20944/preprints202410.2004.v1

Figure 6. Stress distribution along the thickness direction of permanent magnets under different thickness conditions of permanent magnets: (a) Static radial stress; (b) Static tangential stress;(c) Dynamic radial stress;(d) Dynamic tangential stress.

Taking h_{Nd} as 1mm and other conditions unchanged, analyze the influence ofh_{Sleeve} on stress. The range of h_{Sleeve} is 1-4mm.

Figure 7a shows the radial stress distribution of permanent magnet in static state with the increase of h_{Sleeve}. The radial compressive stress increases. Figure 77b shows the tangential stress distribution of permanent magnet in static state with the increase of h_{Sleeve}. The tangential compressive stress increases. It can be seen that increasing h_{Sleeve} can help increase the preload force.

Figure 7c shows the radial stress distribution of permanent magnet in dynamic state, and the radial pressure is somewhat higher than that in static state. Figure 7d shows the tangential stress distribution of permanent magnet in dynamic state, and the tangential pressure is significantly lower than that in static state. With the increase of h_{Sleeve}, the amplitude of change in compressive stress is significantly reduced.

It can be seen that increasing h_{Sleeve} can increase the preload force and reduce the difference between dynamic shear stress and static shear stress, preventing damage to the permanent magnet under dynamic conditions.

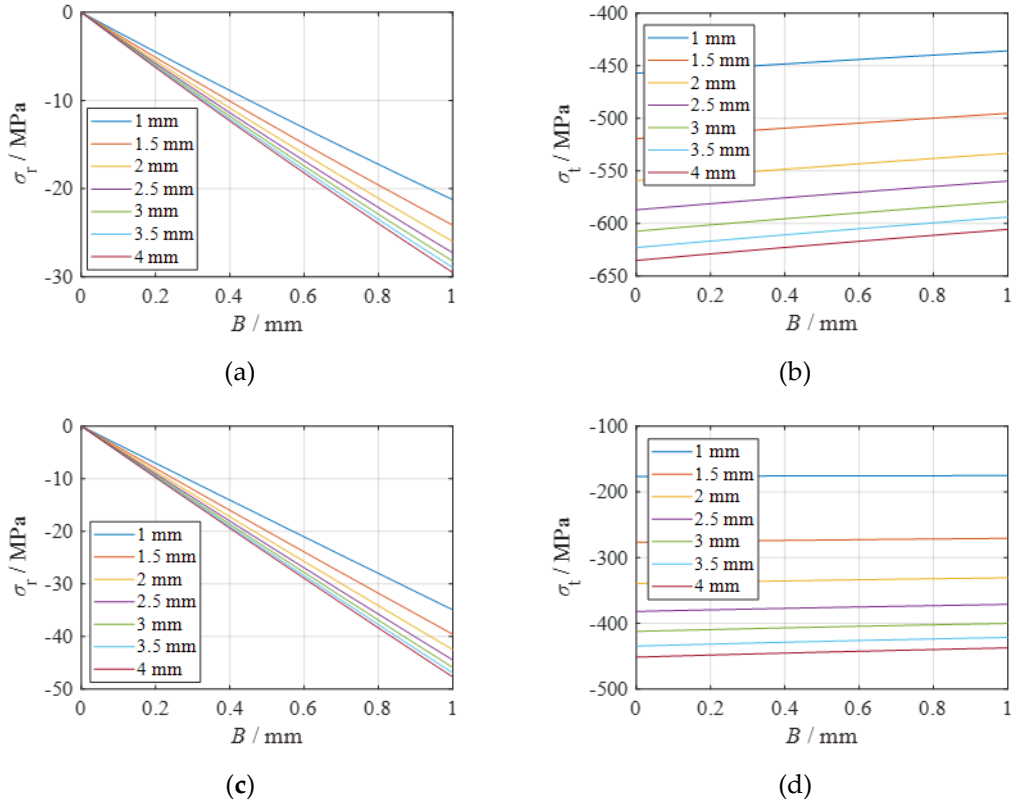

Figure 7. Stress distribution along the thickness direction of permanent magnets under different sleeve thickness conditions: (a) Static radial stress; (b) Static tangential stress;(c) Dynamic radial stress;(d) Dynamic tangential stress.

Taking h_{Sleeve} as 2mm and other conditions unchanged, analyze the influence of interference on stress between permanent magnet and shaft with a range of interference as 0.05-0.2mm.

Figure 8a shows the radial stress distribution of permanent magnet in static state with the increase of interference. The radial compressive stress increases. Figure 8b shows the tangential stress distribution of permanent magnet in static state with the increase of interference. The tangential compressive stress increases significantly. It can be seen that increasing interference can help increase preload force. It should be noted that when interference is greater than or equal to 0.175mm, the

 doi:10.20944/preprints202410.2004.v1

compressive stress exceeds the compression limit of permanent magnet, resulting in damage to permanent magnet.

Figure 8c shows the radial stress distribution of permanent magnet in dynamic state with an increase in interference, and the radial pressure is somewhat higher than that in static state. Figure 8d shows the tangential stress distribution of permanent magnet in dynamic state with an increase in interference, and the tangential pressure is significantly lower than that in static state.

It can be seen that increasing interference can significantly increase preload force and prevent damage to the permanent magnet under dynamic conditions, but it should be noted that too large static compressive stress can cause damage to permanent magnets.

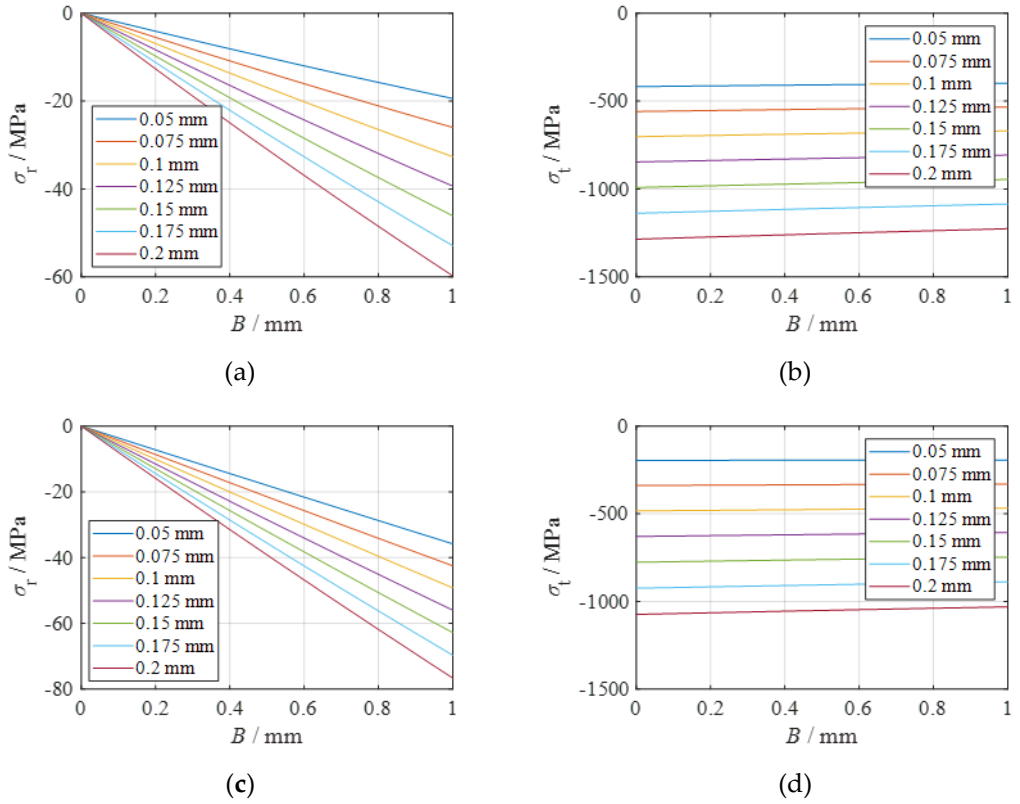

Figure 8. Stress distribution along the thickness direction of permanent magnets under different interference conditions: (a) Static radial stress; (b) Static tangential stress;(c) Dynamic radial stress;(d) Dynamic tangential stress.

Based on the above analysis, it can be concluded that an increase in D will increase centrifugal force-induced tensile stress; an increase in h_{Nd} will significantly increase high-speed tensile stress and cause damage to permanent magnets; an increase in h_{Sleeve} can reduce high-speed centrifugal force on permanent magnet stress; an increase in interference can significantly increase preload compressive stress.

Through calculations, we give limiting conditions as follows:

$$s.t.\begin{cases} 38 \le D \le 42 \\ 1 \le h_{Nd} \le 2 \\ 2 \le h_{Sleeve} \le 3 \\ 40 \le L_{ef} \le 56 \end{cases} \tag{2}$$

The above stress limits meet the strength requirements of the permanent magnet, so the motor performance can be further optimized within this range.

4. Coupled Modeling and Analysis of Electromagnetic Field and Temperature Field in Electric Motors

 doi:10.20944/preprints202410.2004.v1

4.1. Finite Element Modeling of Electromagnetic Fields

Due to the symmetry characteristics of the motor, the 2-D finite element model adopted in this paper can fully meet the accuracy requirements. In order to further reduce the amount of calculation, the 1/2 model is adopted. Figure 9 is the mesh division diagram of the 1/2 Motor 2D finite element model. The mesh division quality is good, and the number of division elements is 8000, which can meet the calculation accuracy and efficiency.

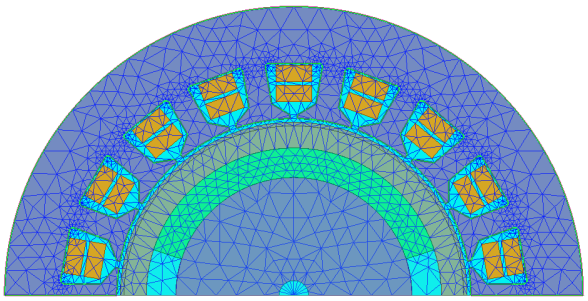

Figure 9. Mesh.

For the two-dimensional electromagnetic finite element model, the potential function is generally used to calculate the electromagnetic field of the motor. The potential function includes magnetic vector potential A and magnetic scalar potential ϕ, so the electromagnetic field problem on the plane field Ω can be expressed as:

$$\begin{cases} \Omega: \dfrac{\partial}{\partial x}\left(\zeta \dfrac{\partial A}{\partial x}\right)+\dfrac{\partial}{\partial y}\left(\zeta \dfrac{\partial A}{\partial y}\right)=-J_Z \\ \Gamma_1: A=A_0 \\ \Gamma_2: \zeta \dfrac{\partial A}{\partial x}=-H_\tau \end{cases} \tag{3}$$

where, ζ is Magnetoresistance, A is magnetic vector potential, only z-axis component, J_Z is Source current density, H_τ is Tangential component of magnetic field intensity, Γ_1 is the first type boundary, Γ_2 is the second type boundary.

$$B_x=\frac{\partial A}{\partial y} \qquad B_y=-\frac{\partial A}{\partial x} \tag{4}$$

The PM adopts the surface current model, as shown in Figure 10. After being magnetized, the PM shall meet the characteristics, as shown in Equation (5). The right end of the equation reflects the excitation characteristics of the PM, as shown in Equation (6), which is the surface current density.

$$\mathrm{rot}\left(\frac{B}{\mu_r \mu_0}\right)=\mathrm{rot}\left(\frac{M_r}{\mu_r}\right) \tag{5}$$

$$J_S=\frac{M_r \times n}{\mu_r} \tag{6}$$

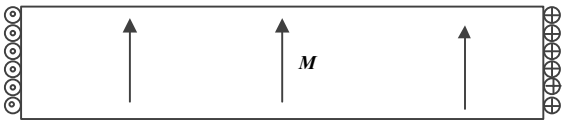

Figure 10. Surface current model of PM.

 doi:10.20944/preprints202410.2004.v1

In this paper, the PM adopts radial magnetization, as shown in Figure 11, the current layer along the BC and AD sides is:

$$J_{SC} = M_{\mathrm{r}} \times n = 0 \tag{7}$$

The current layer along the AB and CD sides is:

$$J_{SC} = J_S \tag{8}$$

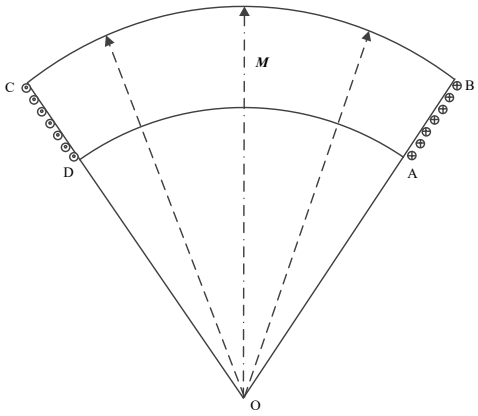

Figure 11. Diagram of radial magnetization.

By solving the electromagnetic field problem, A can be obtained, and then the performance parameters of each cylinder of the motor can be obtained by using A.

The performance parameters of the motor can be obtained by using A. Figure 12 shows the magnetic field cloud diagram of the finite element model of the motor when no load.

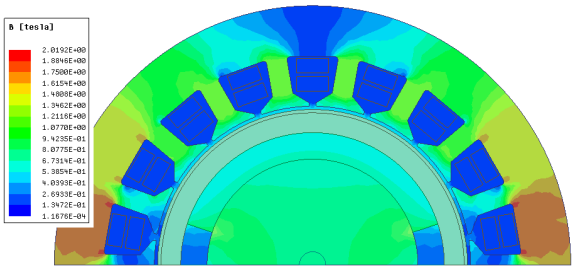

Figure 12. Diagram of radial magnetization.

4.2. Finite Element Modeling of Temperature Field

The ultra-high-speed motor adopts water cooling. The basic assumptions for fluid flow and heat transfer calculations in various regions of the motor are as follows:

(1) Basic assumptions and boundary conditions for fluid flow and thermal coupling calculations in electric machines

(2) Assuming that the upper and lower stator windings are of the same width.

(3) It is believed that the components in the motor are in close contact and have no contact thermal resistance.

(4) Assuming that the heat of the motor is only removed by convection through the fluid in the cooling water jacket, and that there is no heat transfer between the motor and the air.

(5) Ignoring the influence of heat dissipation at the end of the stator.

(6) Due to the high Reynolds number of the fluid inside the water jacket, the flow belongs to turbulent flow. A turbulence model is adopted for the fluid and solved, the fluid is incompressible

 doi:10.20944/preprints202410.2004.v1

Based on the above assumptions, the boundary conditions for the calculation model in this article are as follows:

(1) Since the fluid in the water jacket is incompressible, the rated water velocity is 20L/min, and the inlet temperature is 40°C.

(2) The ambient temperature of the motor is set to 25°C.

(3) All solid surfaces are set as wall boundary conditions, and coupling is added between surfaces to allow temperature transfer.

(4) The heat sources in the motor include the stator teeth, the stator yoke, and the stator winding.

Figure 13 is a mesh division diagram of the finite element model of heat transfer of the motor. The division quality is good and can meet the following temperature field calculation.

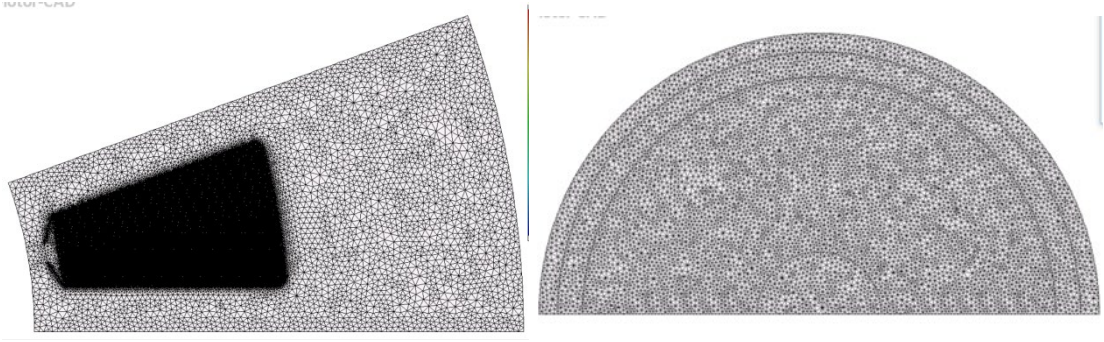

(**a**) (**b**)

Figure 13. Motor grid subdivision: (**a**) stator slot; (**b**) rotor.

In order to obtain the temperature distribution in the medium, it is necessary to solve the heat flow equation in an appropriate form. However, this solution depends on the physical conditions at the boundary of the medium. If the process changes with time, this solution also depends on the internal conditions of the medium at a certain starting time. When it comes to boundary conditions, there are several common physical effects at the boundary, which can be simply expressed in mathematical formulas. In order to determine the temperature distribution inside the object, for the above heat conduction equation, it is necessary to give appropriate boundary conditions. Common boundary conditions are divided into three categories.

(1) Temperature boundary conditions (first type of boundary conditions):

$$\begin{cases} T(x,y,z)|_{S_1} = T_c \\ T(x,y,z)|_{S_1} = f(x,y,z,t) \end{cases} \tag{9}$$

where T_c is the given temperature on the boundary surface S_1, $f(x,y,z,t)$ is a known temperature function, and S_1 is the object boundary.

(2) The boundary condition for heat flow (second type boundary condition):

$$\begin{cases} -\lambda \frac{\partial T}{\partial n}|_{S_2} = q_0 \\ -\lambda \frac{\partial T}{\partial n}|_{S_2} = g(x,y,z,t) \end{cases} \tag{10}$$

where, the heat conduction at the boundary is a known value q_0 (outward), refers to the known normal gradient of the boundary. When $q_0 = 0$, there is no heat conduction on this surface, which is called an adiabatic boundary condition.

In this equation, q_0 represents the boundary heat flow input on the S_2 surface,g(x,y,z,t) is the heat flow density function, and λ is the coefficient of heat conduction perpendicular to the surface of the object.

(3) Thermal exchange boundary condition (third type boundary condition):

 doi:10.20944/preprints202410.2004.v1

The heat flow rate transmitted from the interior of the object to the boundary on boundary S_3 is equal to the heat flow rate dissipated into the surrounding medium through this boundary, This equation is shown below:

$$-\lambda \frac{\partial T}{\partial n}|_{S_3} = \alpha(T - T_0) \tag{11}$$

where T_0 represents the temperature of the surrounding medium, α is the heat transfer coefficient of the S_3 surface, and both T_0 and α can be constants or functions of time and position.

When using the finite element method to calculate temperature rise in an ultra-high speed motor, determining the physical parameters of the model is crucial. Physical properties are all reflected by material properties, so the material must be assigned to each entity. When conducting temperature field analysis, motor materials include parameters such as density, specific heat capacity, and coefficient of heat conduction. The main components in this analysis involve permanent magnets, non-magnetic alloy steel, stator steel laminations, copper windings, insulation, the casing and so on. The following are some material property values:

Table 4. Data sheet of materials used in the model.

Name	material	density (kg/m3)	thermal conductivity (W/m°C)	Specific heat capacity (J/kg°C)
core	Silicon steel sheets	7800	42.5	502.4
winding	copper	8900	387.6	504
Air inside the air gap	Air	1.18	0.026	1042
Permanent magnet protective sleeve	carbon fibre	1600	0.59	1000
PM	NdFeB	8400	8	504
axle	steel	7800	50	504
housing	aluminum alloy	2790	168	833
Slot insulation	Polyimide	1430	0.35	1130

The losses in the motor thermal circuit model are calculated using an electromagnetic model. When the motor speed is 100,000 r/min and the DC bus voltage is 540V with a peak phase current of 35A, the electromagnetic model calculates the iron loss distribution shown in Figure 14. It can be seen that the iron loss mainly occurs around the stator slots, while the rotor loss mainly occurs on the surface of the permanent magnets and iron core. The loss distribution values are shown in Table 5. These losses are directly imported into the motor thermal field model for temperature field simulation calculations.

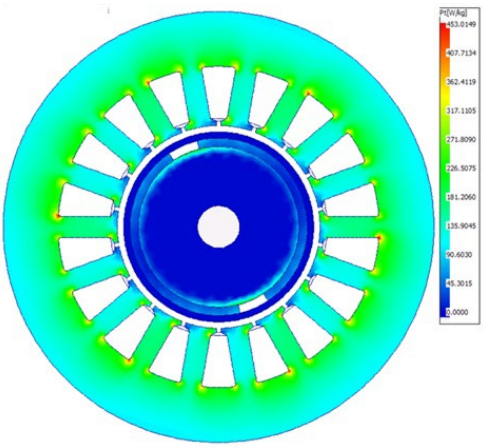

 doi:10.20944/preprints202410.2004.v1

Figure 14. Cloud chart of motor loss distribution.

Table 5. Distribution value of motor loss.

component	loss (W)
Stator yoke	248.4
stator teeth	87.97
Rotor yoke	3.224
PM	3.632
Winding	144.3

Figure 16 show the temperature distribution of the motor calculated using finite element analysis. The high-temperature area is mainly concentrated in the stator winding, with a maximum temperature of no more than 130℃, and a maximum temperature of no more than 120℃ in the rotor area

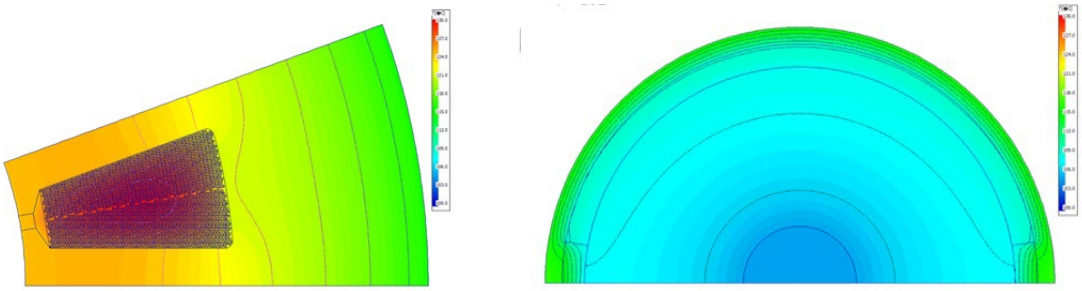

(**a**) (**b**)

Figure 16. Cloud diagram of temperature distribution obtained through finite element calculation: (a) stator; (b) rotor.

4.3. Coupling Modeling

According to the analysis, motor loss is the direct factor causing motor heating, which in turn affects the distribution of motor temperature field; The temperature directly affects the change in internal resistance of the armature winding, and its resistivity can be expressed by formula (12).

$$\rho(T) = \rho_0\left(1 + \alpha(T - T_0)\right) \quad (12)$$

Meanwhile, temperature also affects the residual magnetic density of permanent magnets, thereby reducing the air gap magnetic field of the motor.

Therefore, in the actual model calculation process, the coupling relationship between electromagnetic field and temperature field must be considered to ensure accurate calculation. Based on the electromagnetic field and temperature field models, a coupled model is established with motor losses and temperature as transfer parameters between the two physical fields, as shown in Figure 17.

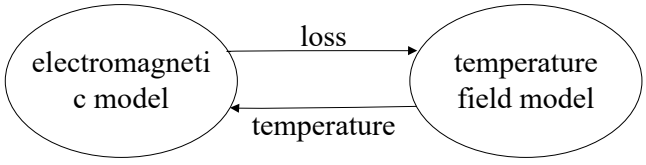

Figure 17. Coupling model of electromagnetic field and temperature field.

Table 6 compares the electromagnetic performance of two models. It can be seen that due to the consideration of the coupling relationship between thermal and electromagnetic fields, the output power calculated by the coupled model is smaller than that of the non coupled model, and the efficiency is also lower. The main reason is that under load, the actual temperature of the motor will

 doi:10.20944/preprints202410.2004.v1

increase. In this case, the temperature of the permanent magnet reached 108.6 °C, and the temperature of the armature conductor reached 122.2 °C, instead of the fixed value of 40 °C given by the uncoupled model, resulting in a decrease in residual magnetism of the permanent magnet from 1.279T to 1.171T. The comparison of the magnetic field cloud map of the motor model is shown in Figure 18, and the air gap magnetic density decreased from 0.5608 T to 0.5213 T. Therefore, under the same current conditions, the power decreases. At the same time, due to the increase in winding temperature (122.2 °C), the phase resistance also increased from the original 0.05814 Ω to 0.07527 Ω, resulting in an increase of about 30W in copper loss. Although the stator iron loss decreased by 50W due to the decrease in magnetic density, the total output power of the motor decreased by nearly 1.2kW, leading to a decrease in overall motor efficiency. It can be seen that the results calculated using the electromagnetic field thermal field coupling model are more realistic and have higher accuracy.

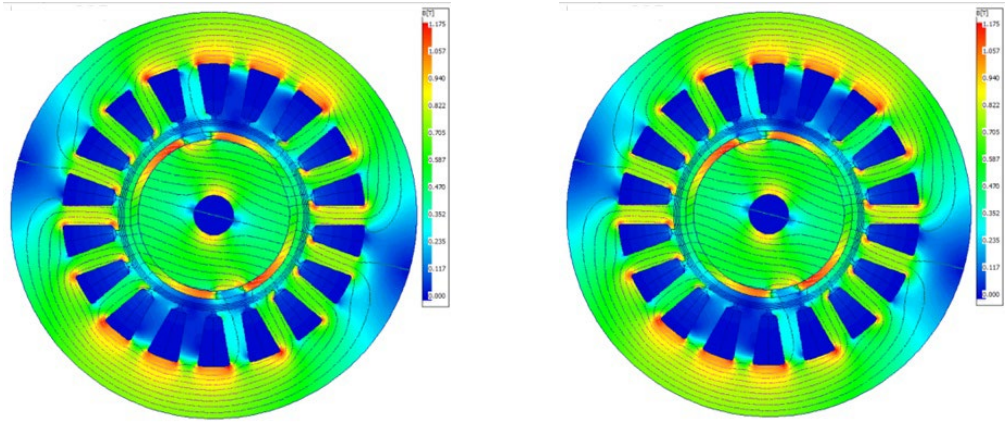

(**a**) (**b**)

Figure 18. Electromagnetic field cloud map: (**a**) Coupling model of electromagnetic and thermal effects; (b) Electromagnetic model.

Table 6. Comparison of electromagnetic performance between two models.

Name	coupled model	Decoupled model
output power (W)	13509	14735
Air gap magnetic density (amplitude) (T)	0.5213	0.5608
Residual magnetization of permanent magnet (T)	1.171	1.279
efficiency (%)	96.609	96.765
Phase Resistance (Ω)	0.07527	0.05814
Armature DC copper loss (W)	138.3	106.8
Stator core loss (W)	329	379
Armature conductor temperature (°C)	122.2	40
rotor temperature (°C)	107.5	40

5. Coupling Model Based on Mechanical Field Limitations

5.1. Coupling Modeling

Considering that the deformation caused by the force on the motor structure is very small and has little effect on the electromagnetic field, the main consideration is the dynamic characteristics of the motor rotor at high speeds.

Therefore, the design of the motor rotor follows the following principles:

Preprints.org (www.preprints.org) | NOT PEER-REVIEWED | Posted: 25 October 2024 doi:10.20944/preprints202410.2004.v1

(1) Determine the limit value of the outer radius of the permanent magnet based on the surface speed requirements of the rotor.

(2) According to the strength requirements of the rotor, determine the thickness of the protective sleeve h_{sleeve} and the interference amount $\delta_s$restriction.

(3) Determine the outer rotor diameter and axial length limit values based on the stiffness and critical speed of the rotor.

Then, the size limit value is used as a constraint condition for the optimization design model, and a multi physics field coupling optimization model for the motor is established, as shown in Figure 19.

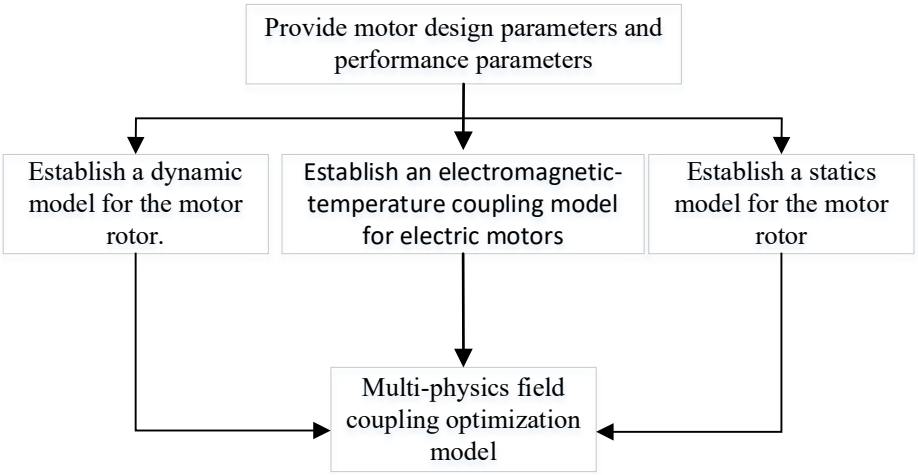

Figure 19. Coupling model of electromagnetic field and temperature field.

5.2. Parametric Design of Coupled Models

In order to optimize the design of the motor, the established coupling model was parameterized and the range of parameter values was determined based on the previous analysis. The specific design parameters include: cooling system parameters (h_{duct},h_{Jacket},b_{duct}), Overall dimensions of motor (D_{o1},D,L_{ef},h_{Sleeve},L_{Airgap}), permanent magnet parameters (h_{Nd},$b_{embrace}$), internal parameters of the stator ($bs0$,h_{tooth},$hs0$, Ang,$hs2$,$r1$), and winding parameters ($Nstrands$,I_{phase}). Dimensional limitations are imposed on the outer diameter of the rotor core, armature length, and sleeve thickness based on mechanical properties, as shown in equation (28).

As shown in Table 7, the main performance parameters of the motor are: motor efficiency (η), output power(P_{out}),cogging torque(T_{cog}),maximum winding temperature ($T_{coilMax}$), and power density (k_p).

Table 7. Optimize the range of design parameters.

	Name	Variable	Unit	Range
Cooling system parameters	Sink height	h_{duct}	mm	2-10
	Wall thickness of water jacket	h_{Jacket}	mm	1-3
	Sink span	b_{duct}	mm	6-12
	Coolant flow rate	v_0	L/min	
Overall dimensions of motor	Outer diameter of stator	D_{o1}	mm	110-130
	Outer diameter of rotor core	D	mm	38-42
	Armature length	L_{ef}	mm	40-56
	Sleeve thickness	h_{Sleeve}	mm	1-3

 doi:10.20944/preprints202410.2004.v1

	Air gap length	L_{Airgap}	mm	0.3~1.5
PM parameters	Thickness of permanent magnet	h_{Nd}	mm	1-2
	Permanent magnet width	$b_{embrace}$	°	140-180
Internal parameters of the stator	Slot opening	bs0	mm	1-4
	tooth width	h_{tooth}	mm	3-7
	Shoulder height of slot	hs0	mm	0.3-3
	Slot Shoulder angle	Ang	°	15-30
	slot depth	hs2	mm	12-18
	Radius of slot bottom corner	r1	mm	0.5-2
Winding parameters	Number of parallel windings	Nstrands		280-340
	Phase current	I_{Phase}	A	
Motor performance	Efficiency	η	%	
	Output power	P_{out}	kW	
	Cogging torque	T_{cog}	Nm	
	Maximum temperature of winding	$T_{coilMax}$	°C	
	Spacer factor	k_s	%	
	Power density	k_p	kW/kg	

6. Optimized Design of High-Speed Motor

When dealing with the optimization of electric motors, numerous objectives and design parameters frequently arise. Nevertheless, establishing precise, explicit formulas linking these design parameters to the optimization objectives is often infeasible. Typically, the intricate relationship between them is derived through finite element simulation calculations, a process referred to as constructing a surrogate model, as illustrated in Figure 20.

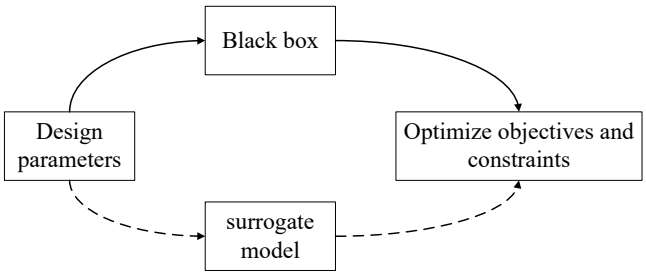

Figure 20. Schematic diagram of surrogate model.

6.1. Optimization Model

With the optimization objectives of maximizing efficiency and power density, while simultaneously limiting cogging torque, slot fill factor, maximum temperature rise of windings, and output power, the optimization model is presented in Equation (13), and the design parameters are shown in Equation (14). The range of values for each design parameter is illustrated in Table 7.

 doi:10.20944/preprints202410.2004.v1

$$\max y = \{\eta(x), \quad k_p(x)\}$$
$$s.t. \begin{cases} T_{cog}(x) \le 0.00015 \\ k_s \le 0.8 \\ T_{coilMax} \le 140 \\ 14000 \ge P_{out} \ge 12000 \\ x_i^1 \le x_i \le x_i^2 \end{cases} \tag{13}$$

$$x = \begin{Bmatrix} bs0, b_{embrace}, L_{Airgap}, h_{Nd}, h_{Sleeve}, L_{ef}, D_{O1}, \\ h_{tooth}, D, I_{Phase}, h_{Jacket}, Nstrands, hs0, hs2 \end{Bmatrix} \tag{14}$$

6.2. Optimization Process

Based on the ultra-high-speed motor model that couples electromagnetic and thermal fields, an optimization design algorithm based on a surrogate model is adopted to optimize the design of the ultra-high-speed motor. The specific optimization process is shown in Figure 21. Firstly, the electromagnetic-thermal coupling model is used to conduct sensitivity analysis of the motor, providing parameters for motor optimization design. At the same time, constraints on motor design parameters are given based on the analysis of the motor's mechanical field. Then, an optimization design model based on multi-physical field coupling is established. MaxPro experimental design is used to obtain initial samples. After calculation using the multi-physical field coupling model, a surrogate model is fitted using Kriging. Based on this surrogate model, genetic algorithms are used for optimization design, and the optimization results are verified. If the requirements are not met, new samples are added to rebuild a New Kriging Surrogate model and perform optimization design until the accuracy is met.

 doi:10.20944/preprints202410.2004.v1

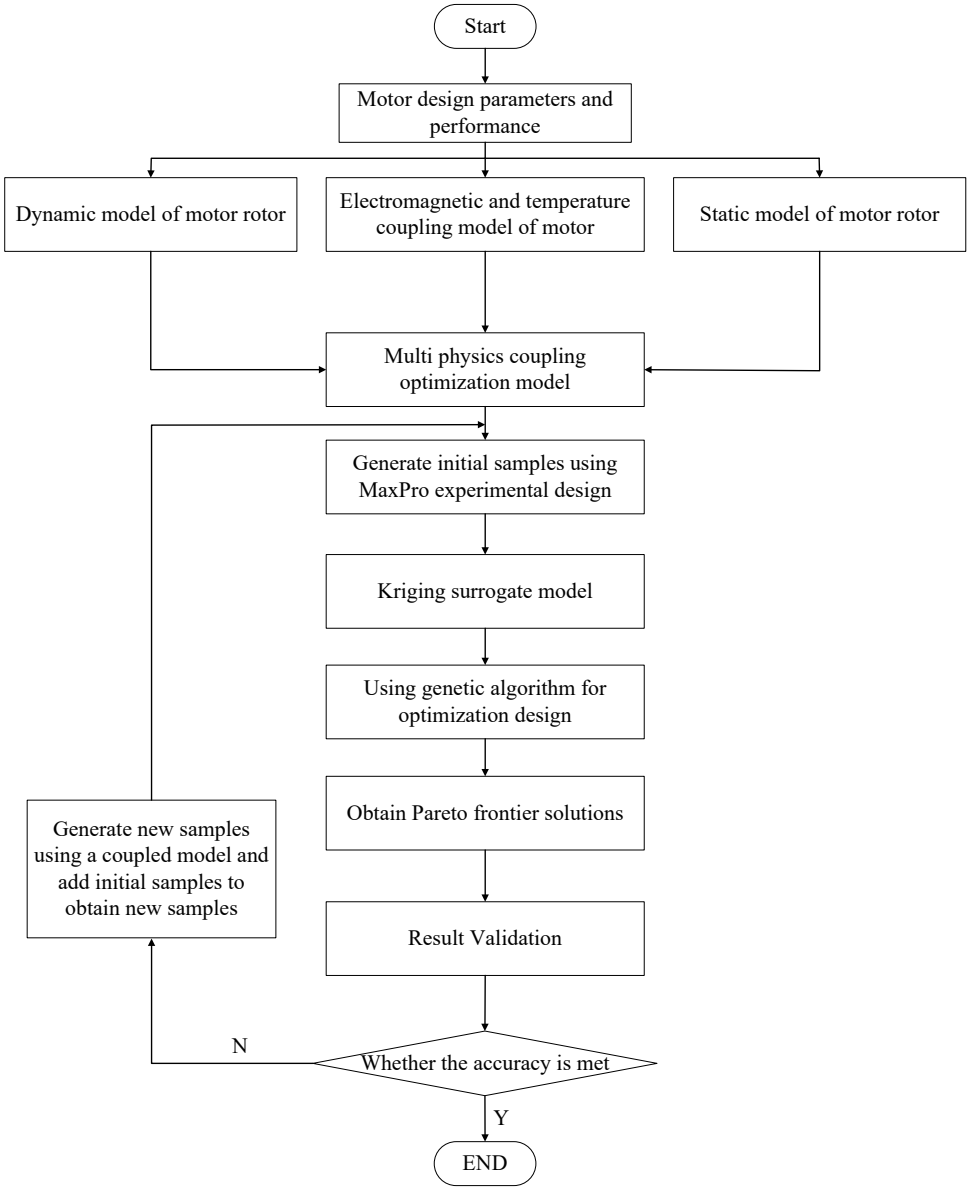

Figure 21. Optimization design process based on multi-physical field coupling.

6.2.1. Experimental Design

In 2015, Joseph, Gul, and Ba introduced a Maximum Projection (MaxPro) experimental design that incorporates a weight factor to guarantee accurate predictions across all subspaces[32]. The underlying concept is outlined as follows:

$$\min_{D} \sum_{i=1}^{n-1} \sum_{j=i+1}^{n} \frac{1}{d^{k}\left(x_i, x_j; w\right)} p(w) dw \tag{15}$$

$$d\left(x_i, x_j; w\right) = \left(\sum_{l=1}^{p} \mathrm{w_{il}} \left| \mathrm{x_{il}} - \mathrm{x_{jl}} \right|^{\mathrm{s}} \right)^{1/\mathrm{s}} \tag{16}$$

where, $\mathrm{w} = \left(\mathrm{w}_1, \cdots, w_p\right)$, $\sum_{l=1}^{p} w_l = 1$, $w_1, \cdots w_l > 0$,w_l is the weight, $p(w)$ represents the priority distribution factor of the weight. When w is uniformly distributed and $w = s \times p$, formula (15) can be simplified to formula (17), where s is typically set to 2.

Preprints.org (www.preprints.org) | NOT PEER-REVIEWED | Posted: 25 October 2024 doi:10.20944/preprints202410.2004.v1

$$d \min_{D} \sum_{i=1}^{n-1} \sum_{j=i+1}^{n} \frac{1}{\prod_{l=1}^{p} \left| x_{il} - x_{jl} \right|^{s}} \tag{17}$$

The MaxPro experimental design does not rely on an even spacing distribution; instead, it aims to reach the boundaries as extensively as possible, making it exceptionally well-suited for surrogate models with a high number of dimensions.

Figure 22 depicts the partial factor distribution of the initial 500 samples acquired through the MaxPro experimental design. It illustrates that the samples are spread uniformly across the entire design space, ensuring comprehensive coverage.

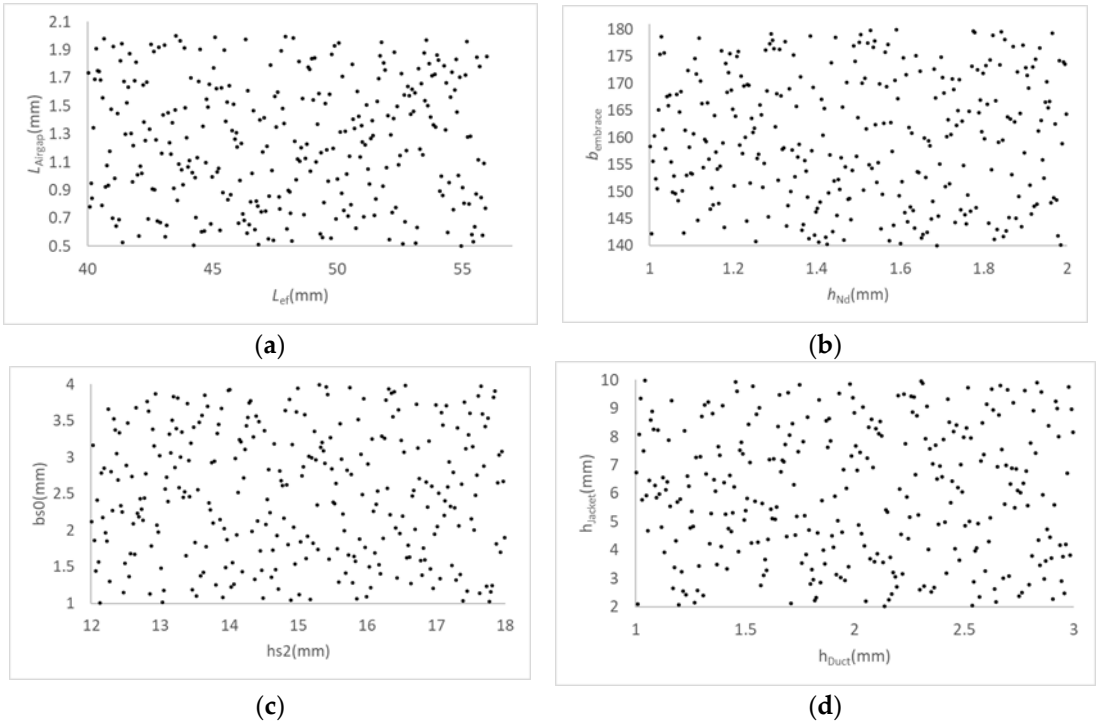

Figure 22. Partial factor distribution: (a) L_{Airgap} vs L_{ef}; (b) $b_{embrace}$ vs h_{Nd};(c) bs0 vs hs2;(d) h_{Jacket} vs h_{Duct}.

6.2.2. Kriging Surrogate Model

The Kriging model, illustrated in equation (18), integrates a global model with local deviations. Due to its exceptional global approximation and error estimation abilities, it is particularly well-suited for addressing nonlinear problems[33].

$$y(x) = f(x) + z(x) \tag{18}$$

where, x represents the design parameter, $y(x)$ denotes the response function, $f(x)$ employs a global approximation model of polynomial response surface, and $z(x)$ signifies local error.

Among them, $z(x)$ represents a static Gaussian random process with an expected value of 0 and a variance ofσ^2. The covariance is shown in (19).

$$Cov\left[z(x_i), z(x_j) \right] = \sigma^2 \mathbf{R}\left[R(x_i, x_j) \right] \tag{19}$$

where, $\boldsymbol{R}$ represents the correlation matrix, and $R(x_i, x_j)$ denotes the correlation function between two samples.

Using the Gaussian correlation function, as shown in equation (20)

 doi:10.20944/preprints202410.2004.v1

$$R(x_i, x_j) = exp\left(-\sum_{k=1}^{m} \theta_k \left| x_{ik} - x_{jk} \right|\right) \tag{20}$$

where, m represents the number of design parameters, and θ_k denotes the unknown correlation coefficient used for fitting the approximate model.

The estimated value at x is:

$$\hat{y} = \hat{\beta} + r^T(x)\mathbf{R}^{-1}\left(y - \mathbf{f}\hat{\beta}\right) \tag{21}$$

where, $\boldsymbol{f}$ represents a unit column vector of length n, y denotes the response column vector of n sample points, and $r^T(x)$ signifies the correlation vector between the n sample points and x. Among them:

$$r(x) = \left[R(x, x_1), R(x, x_2), \cdots, R(x, x_n)\right] \tag{22}$$

$$\hat{\beta} = \left(\mathbf{f}^T\mathbf{R}^{-1}\mathbf{f}\right)^{-1}\mathbf{f}^T\mathbf{R}^{-1}y \tag{23}$$

The estimated variance is:

$$\hat{\sigma}^2 = \frac{\left(y - \mathbf{f}\hat{\beta}\right)\mathbf{R}^{-1}\left(y - \mathbf{f}\hat{\beta}\right)}{n} \tag{24}$$

The maximum likelihood estimation used for the Kriging model is:

$$\max \Phi(\theta_k) = \frac{n\ln\left(\hat{\sigma}^2\right) + \ln|\mathbf{R}|}{2} \tag{25}$$

The Kriging approximation model is obtained by solving the unconstrained optimization problem using numerical optimization algorithms.

Establish a Kriging surrogate model that maps design parameters to motor performance, as shown in equation (26)

$$\begin{cases} x = \begin{Bmatrix} bs0, b_{embrace}, L_{Airgap}, h_{Nd}, h_{Sleeve}, L_{ef}, D_{o1}, \\ h_{tooth}, D, I_{Phase}, h_{Jacket}, Nstrands, hs0, hs2 \end{Bmatrix} \\ \left[k_p, k_s, \eta, P_{out}, T_{cog}, T_{coilMax}\right] = F(x) \end{cases} \tag{26}$$

Relative Maximum Absolute Error (RMAE) and Relative Average Absolute Error (RAAE) are adopted as evaluation metrics for the optimization model. The calculation formulas for RAAE and RMAE are shown in Equations (27) and (28), respectively.

$$\text{RAAE} = \frac{\frac{1}{N}\sum_{i=1}^{N}|y_i - \hat{y}_i|}{\sqrt{\frac{1}{N-1}\sum_{i=1}^{N}(y_i - \hat{y}_i)^2}} \tag{27}$$

$$\text{RMAE} = \frac{\frac{1}{N}\underset{i=1:N}{max}(|y_i - \hat{y}_i|)}{\sqrt{\frac{1}{N-1}\sum_{i=1}^{N}(y_i - \hat{y}_i)^2}} \tag{28}$$

where, N represents the number of test points, y_i denotes the true value of the i^{th} test point, and $\hat{y}_i$ signifies the predicted value of the i^{th} test point.

RMAE and RAAE serve as metrics to assess the local and global precision of the model, respectively. Lower values indicate higher model accuracy.

Figure 23 displays partial outcomes from fitting the Kriging surrogate model. While the surrogate model generally captures the global traits of the samples, its local prediction accuracy is moderate, as depicted in Figure 24. Specifically, the RAAE is below 1 and the RMAE is close to 0. Hence, during the optimization design process, it is crucial to conduct adaptive iterations on the samples to enhance accuracy.

 doi:10.20944/preprints202410.2004.v1

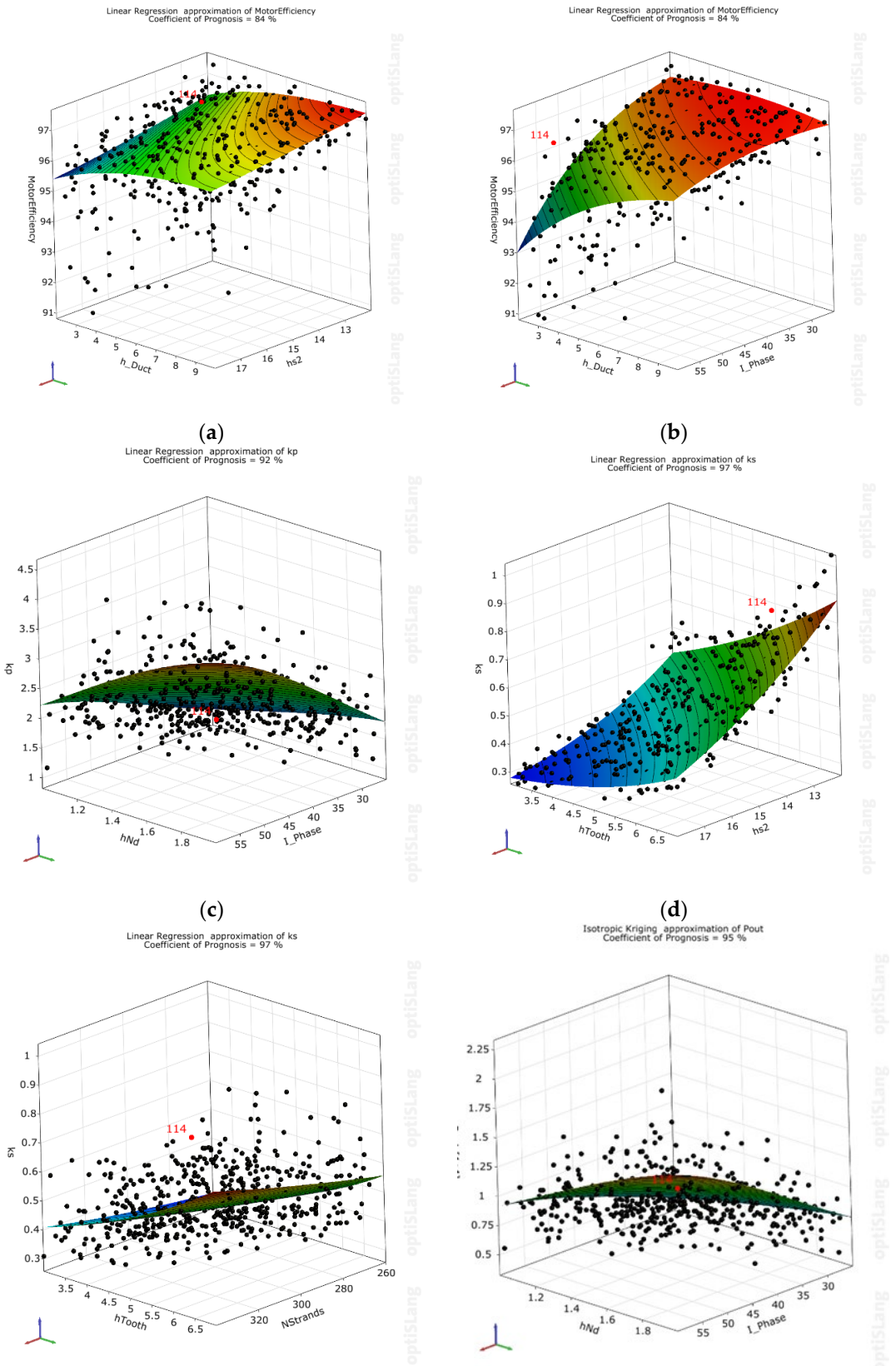

Figure 23. Partial fitting surface of Kriging model (a) η VS h_{Duct}, h_{s2}; (b) η VS h_{Duct}, I_{Phase};(c) k_P VS h_{Nd}, I_{Phase};(d) k_s VS h_{Tooth}, h_{s2};(e) k_s VS h_{Tooth}, $NStands$;(f) P_{out} VS h_{Nd}, I_{Phase}.

 doi:10.20944/preprints202410.2004.v1

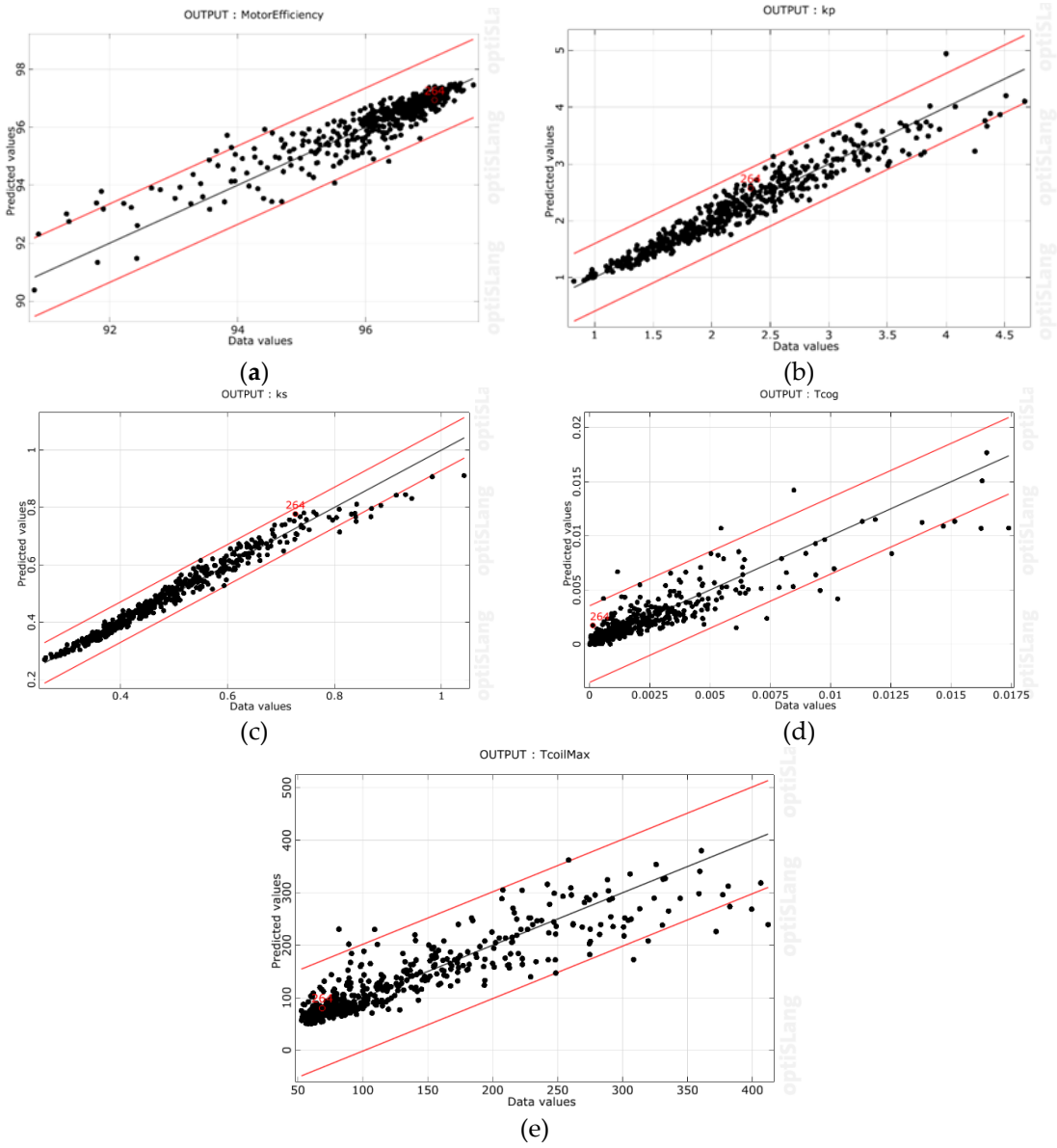

Figure 24. Prediction accuracy: (a) RAAE and RMAE of η are 0.692, 0.0085; (b) RAAE and RMAE of $k_p$are 0.731, 0.01;(c) RAAE and RMAE of k_s=0.707 =0.011;(d) RAAE and RMAE of T_{cog} are 0.587, 0.011;(e) RAAE and RMAE of $T_{coilMax}$ are 0.638, 0.01.

6.2.3. NSGA-2

The schematic diagram of NSGA-2 algorithm is shown in Figure 25 [34]. Its main features are: using fast sorting based on Pareto dominance level can quickly calibrate the dominance level of each individual in the population, and using crowding distance instead of fitness sharing mechanism can obtain a uniformly distributed Pareto optimal solution set. At the same time, using elite retention mechanism can make it easier to obtain excellent next generation. Among them, the crowding distance, as shown in equation (29), is the average value of the Euclidean distance.

$$PCD(p_k) = \frac{1}{m}\sum \frac{f_i(p_{k+1}) - f_i(p_{k-1})}{f_i^{max} - f_i^{min}} \tag{29}$$

where, $f(p_{k+1})$, $f(p_k)$, and $f(p_{k-1})$ are three consecutive Pareto front points and p_{k+1}, p_k, p_{k-1} are the correspond ding Pareto solution; And f_i^{min}, f_i^{max} are the minimum and maximum values of the i^{th} objective function of the Pareto front, respectively.

 doi:10.20944/preprints202410.2004.v1

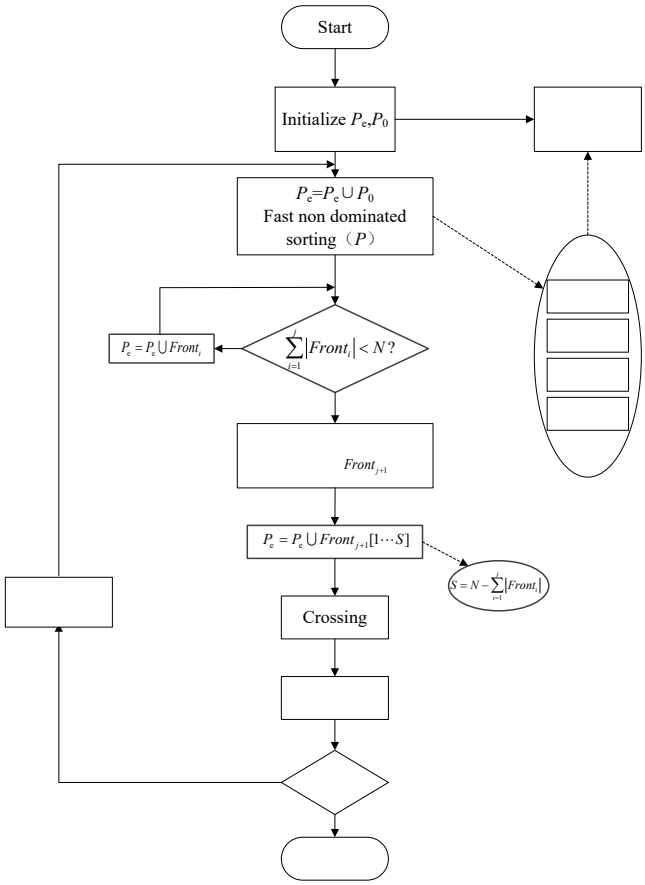

Figure 25. NSGA-2.

6.2.4. Optimization Result Analysis

The MaxPro design is utilized to obtain an initial set of 500 samples. The number of correction points amounts to 50, while there are 200 non-dominant solutions considered. The process involves 500 iterations, and the convergence criteria has been set as

$$\begin{cases} RMAE \leq 0.01 \\ RAAE \leq 0.1 \end{cases} \tag{30}$$

Figure 26. shows that the RMAE and RAAE of the output parameters are less than 0.01 and 0.1 at the fifth generation, and the samples are only 750.

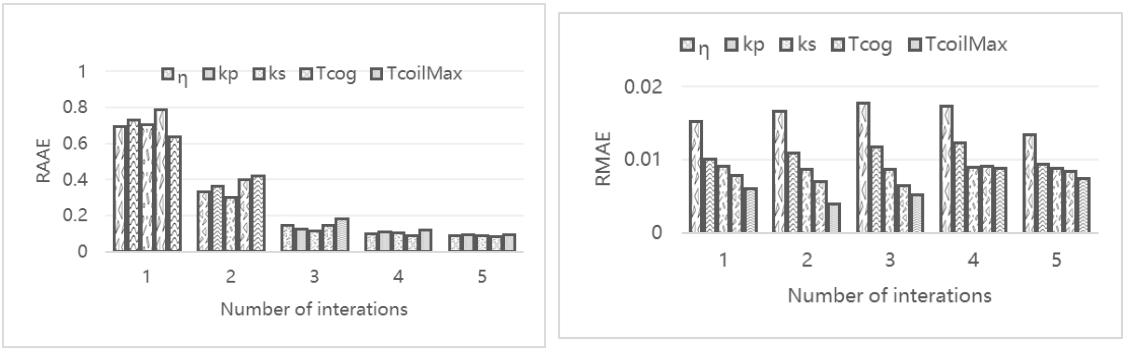

(a) (b)

Figure 26. Convergence process. (a) RAAE. (b) RMAE.

Figure 27 shows the optimized Pareto front, as indicated by the red line in the figure. In this project, five schemes were selected from the Pareto front according to different requirements, as

 doi:10.20944/preprints202410.2004.v1

shown in Table 8. The performance parameters achieved the optimization design goals, with efficiency reaching 97% and power density exceeding 4kW/kg.

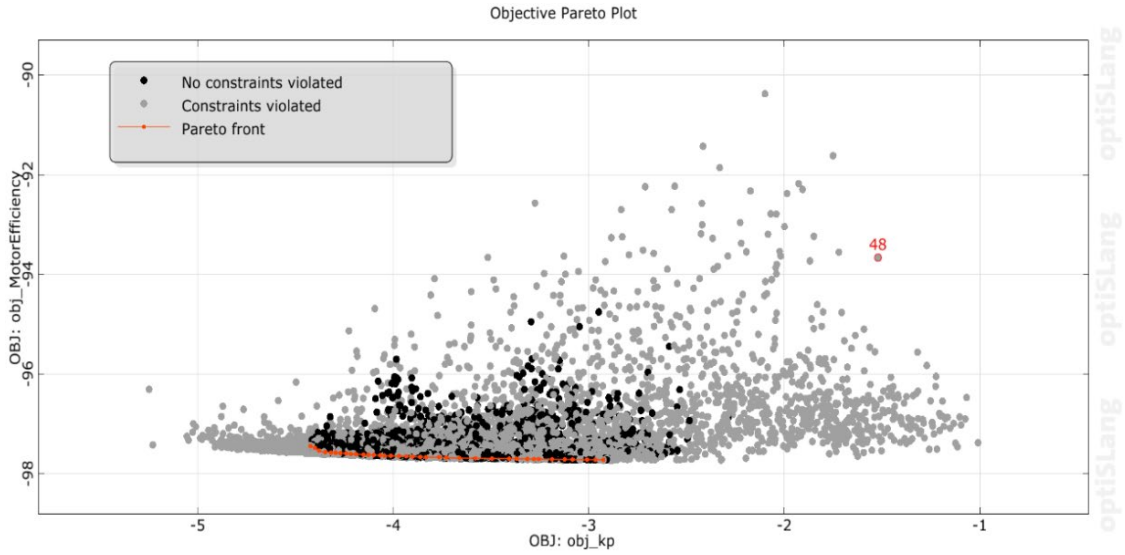

Figure 27. Pareto Frontier.

Table 8. Five designs.

parameter	case1	case2	case3	case4	case5
h_{Sleeve}	2.17	2.20	2.13	2.12	2.17
NStrands	340	340	340	340	340
D_{O1}	110.24	110	130	110	116.6
h_{Jacket}	1.5	1.5	1.5	1.5	1.5
b_{duct}	9	9	9	9	9
L_{ef}	40	40	41.75	45.75	40
L_{Airgap}	0.5	0.5	0.5	0.5	0.5
h_{Duct}	10	8.19	10	8.98	9.98
b_{Throw}	9	9	9	9	9
h_{Nd}	2	2	2	2	2
r_1	1	1	1	1	1
$b_{embrace}$	179.44	180	180	163.64	178.39
hs2	14	14	14	14	14
bs0	1.32	1	1.01	1.64	1.18
Ang	30	30	30	30	30
hs0	0.625	0.719	0.774	0.85	0.68
h_{Tooth}	6.22	6.39	6.42	6.45	6.46
D	41.99	41.82	42	41.97	41.95
I_{Phase}	48.72	48.72	43.30	48.26	48.72
η	97.55	97.44	97.72	97.52	97.64
P_{out}	12998.08	12994.38	12266.47	13941.6	12992.84
T_{cog}	0.00269	0.00055	0.0005	0.0028	0.0027
$T_{coilMax}$	94.96	105.79	87.52	87.39	94.76
k_p	4.349	4.423	3.983	4.406	4.006
k_s	0.767	0.792	0.788	0.8	0.794

Then, finite element analysis was used to verify the accuracy of the five optimization schemes. The verification results are shown in Table 9. The efficiency error of the five optimization schemes is within 1%, and the power density error does not exceed 7%, which meets the requirements. Consider

Preprints.org (www.preprints.org) | NOT PEER-REVIEWED | Posted: 25 October 2024 doi:10.20944/preprints202410.2004.v1

the efficiency and power density of the motor comprehensively, case 2 is chosen as the final design solution.

Table 9. This is a table. Tables should be placed in the main text near to the first time they are cited.

Cases		η	k_p
case1	Optimize design values	97.03	4.349
	Model calculation value	97.556	4.1
	error	0.54%	-6.07%
case2	Optimize design values	97.44	4.4232
	Model calculation value	96.95	4.23052
	error	-0.5%	-4.55%
case3	Optimize design values	97.72	3.983
	Model calculation value	96.99	4.18
	error	-0.74%	4.71%
case4	Optimize design values	97.52	4.41
	Model calculation value	97.133	4.27
	error	-0.39%	-3.28%
case5	Optimize design values	97.64	4.0
	Model calculation value	97.28	3.78
	error	-0.37%	-5.82%

6.3. Motor Performance

Simulation calculations were performed on the final design case with a working bus voltage of 540V and sinusoidal drive. The final power MAP and efficiency MAP of the motor are shown in Figures 28 and Figures 29. The maximum motor speed is 150000r/min, and the highest efficiency reaches 97%, with over 90% accounting for over 80%.

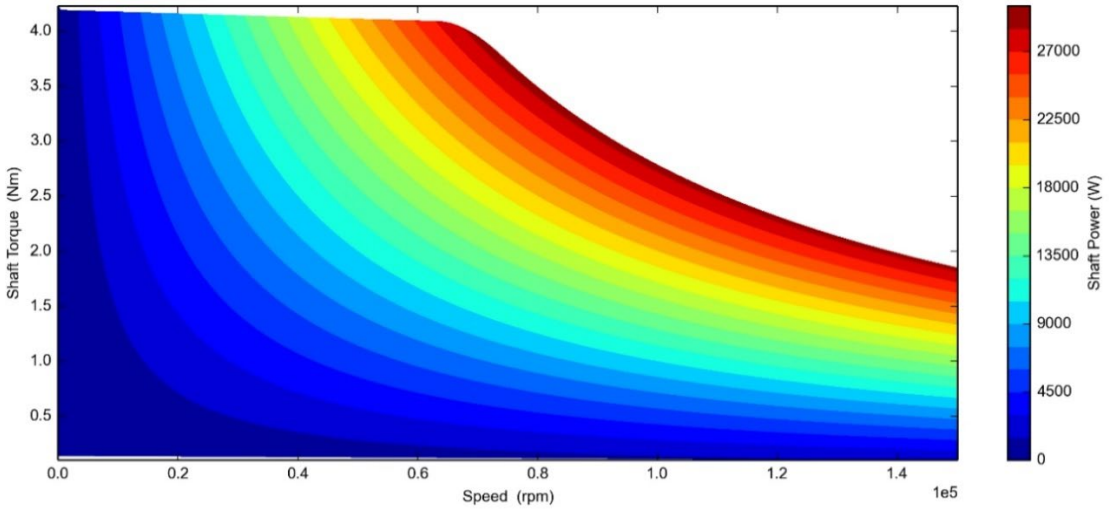

Figure 28. MAP of motor power.

 doi:10.20944/preprints202410.2004.v1

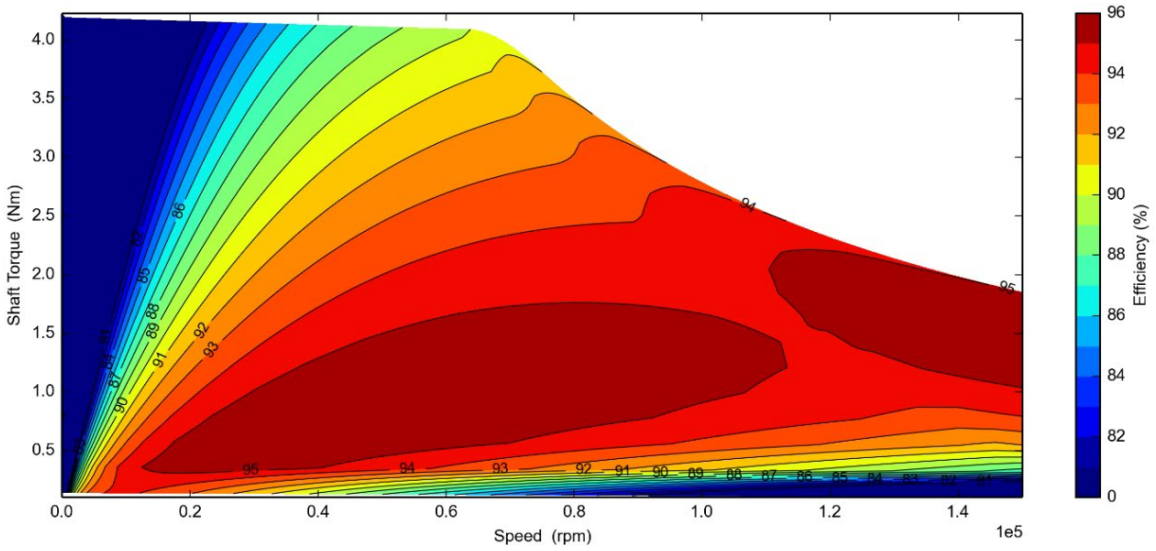

Figure 29. MAP of motor efficiency.

7. Experiments and Verification

Due to the inability to find testing equipment for this type of ultra high speed motor on the current market, this project plans to adopt a simplified testing scheme to indirectly complete motor performance testing, as shown in Figure 30. The measurement and control system sets the controller speed, and the controller controls the compressor to operate at the given speed. The measurement and control system measures the inlet and outlet pressures of the compressor to calculate the pressure ratio. The power consumption of the compressor is indirectly calculated through the pressure difference and flow rate according to equation (31). At the same time, the measurement and control system needs to test the motor voltage and current to calculate the electric power (P_e). The motor efficiency is calculated according to equation (32), where η_c is the motor controller efficiency.

$$P_{Air} = \Delta p \times v_{Air} \times \eta_{Air} \tag{31}$$

$$\eta_{motor} = \frac{P_{Air}}{P_e} \times \frac{1}{\eta_c} \times 100\% \tag{32}$$

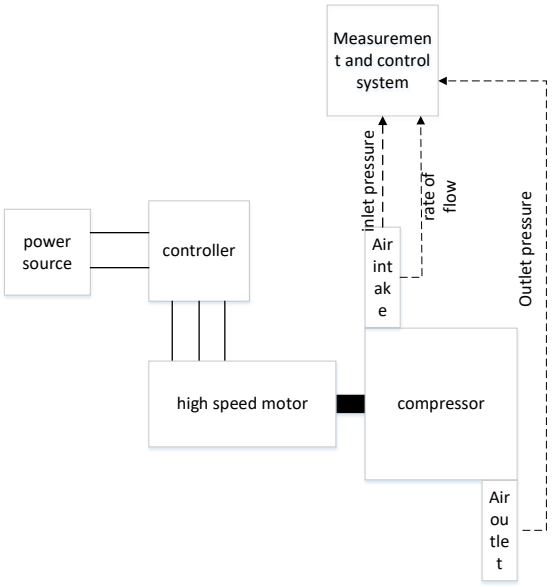

Figure 30. Principle Block Diagram of the test Platform.

 doi:10.20944/preprints202410.2004.v1

Table 10 shows the mass of each part of the two motors, designed according to a rated power of 12kW, with a power density of 4kW/kg.

Table 10. Motor power density.

Name	weight	
	JQHM-SZ22010001	JQHM-SZ22010002
stator core (kg)	1.41	1.43
rotor (kg)	0.56	0.53
PM (kg)	0.084	0.081
winding (kg)	0.87	0.85
total (kg)	2.924	2.911
power density (kW/kg)	4.1	4.12

A testing platform was built according to Figure 30 as shown in Figure 31, and ultra high speed motor performance tests were conducted on both motors. During the test, the temperature was controlled at 20~35 °C , and the atmospheric pressure was controlled at 101kPa.

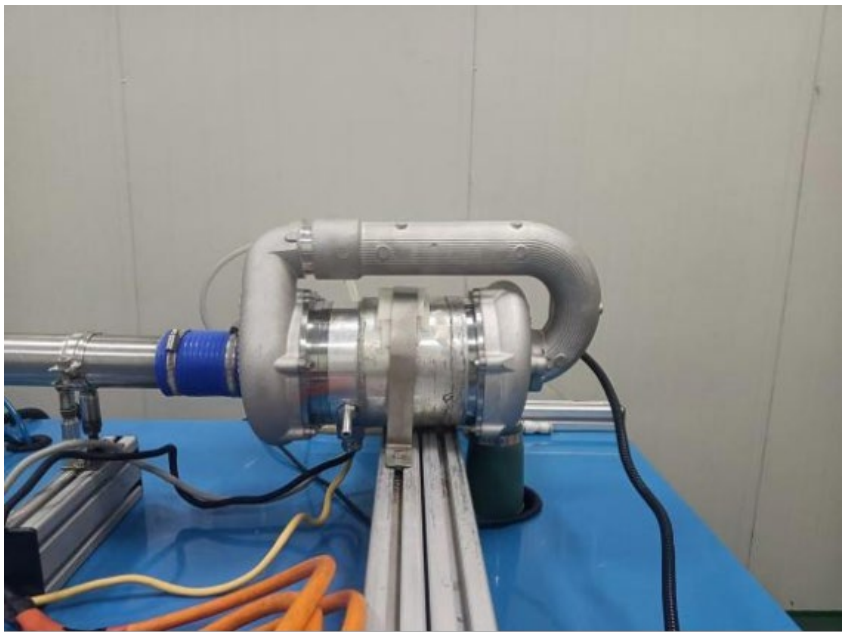

Figure 31. Motor testing bench.

The test data of JQHM-SZ22010001 motor is shown in Table 11, and the test data of JQHM-SZ22010002 motor is shown in Table 12. If the efficiency of the motor controller is estimated at 96%, the actual efficiency of the motor can be obtained. It can be seen that the efficiency of both motors can exceed 95% at around 12kW, meeting the design specifications, and the efficiency is also close to 95% at 8kW power.

Table 11. Experimental data of JQHM-SZ22010001.

speed (r/min)	Imported water temperature (°C)	Outlet water temperature (°C)	Air compressor pressure ratio	mass flow (g/s)	Air compressor power consumption (kW)	average current (A)	voltage (V)	motor temperature (°C)	efficiency (%)
50000	23.13	35.75	1.162	80.3	5.725	11.7	538	46	94.7
60000	21.72	41.81	1.271	89.8	6.843	14.0	536	53	95

 doi:10.20944/preprints202410.2004.v1

70000	21.75	49.32	1.453	99.1	7.986	16.4	535	64	94.7
80000	21.92	51.91	1.876	119.2	9.128	18.7	535	74	95.2
90000	21.5	61.06	1.932	139.4	10.271	21.0	534	81	95.4
100000	21.8	66.72	2.201	154.5	11.446	23.2	534	97	96.25

Table 12. Experimental data of JQHM-SZ22010002.

speed (r/min)	Imported water temperature (°C)	Outlet water temperature (°C)	Air compressor pressure ratio	mass flow (g/s)	Air compressor power consumption (kW)	average current (A)	voltage (V)	motor temperature (°C)	efficiency (%)
50000	22.19	36.14	1.153	79.8	5.736	11.7	539	48	94.7
60000	21.9	44.47	1.266	90.6	6.866	14.0	537	56	95.1
70000	21.81	56.74	1.465	98.5	7.988	16.4	536	62	94.65
80000	21.92	60.59	1.881	121.6	9.132	18.7	535	73	95
90000	21.87	63.42	1.945	143.6	10.280	21.0	534	81	95.5
100000	21.74	70.2	2.212	155.7	11.451	23.2	534	97	96.3

8. Conclusion

The research on optimal design of ultra-high-speed motors based on multi-physical field coupling under mechanical boundary constraints has achieved remarkable results. By comprehensively considering electromagnetic, thermodynamic, and mechanical interactions, a precise model was established to simulate motor performance. This enabled the investigation of various design parameters and their impact on motor efficiency and power density. The proposed optimization method, combining experimental design, surrogate modeling, and evolutionary algorithms, significantly improved motor performance while adhering to mechanical constraints. The findings offer valuable insights and guidance for the design and development of ultra-high-speed motors, contributing to advancements in related fields.

Author Contributions: Conceptualization, Jianguo Bu; Data curation, Jianguo Bu and Weifeng Zhang; Formal analysis, Yan Yu; Funding acquisition, Hailong Pang; Investigation, Jianguo Bu and Yan Yu; Methodology, Jianguo Bu and Weifeng Zhang; Project administration, Jianguo Bu; Resources, Hailong Pang and Wei Lei; Software, Yan Yu and Wei Lei; Supervision, Hailong Pang; Validation, Yan Yu; Visualization, Yan Yu; Writing – original draft, Jianguo Bu; Writing – review & editing, Weifeng Zhang, Yan Yu and Wei Lei. All authors have read and agreed to the published version of the manuscript.

Funding: This research was funded by Tianjin Key Research and Development Program Technology Support Project, grant number 20YFZCGX00760.

Data Availability Statement: Not applicable.

Acknowledgments: Not applicable.

Conflicts of Interest: Not applicable.

References

1. ZHANG Fengge, DU Guanghui, WANG Tianyu, et al. Review on Development and Design of High Speed Machines [J]. TRANS ACTIONS OF CHINA ELECT R OTECHNICAL SOCIETY, 2016, 31(7):18.DOI:10.3969/j.issn.1000-6753.2016.07.001.
2. Berton J J, Kim H D, Singh R, et al. Turboelectric Distributed Propulsion Benefits on The N3-X Vehicle[J]. Aircraft Engineering and Aerospace Technology: An International Journal, 2014, 86 (6): 558-561.
3. Clarke S, Lin Y, Kloesel K, et al. Enabling Electric Propulsion for Flight-Hybrid Electric Aircraft Research at AFRC[C]. Atlanta: AIAA Aviation Technology, Integration, and Operations Conference, 2014.
4. Welstead J, Felder J, Guynn M, et al. Overview of the NASA STARC-ABL (rev. B) Advanced Concept[C]. Washington:One Boeing NASA Electric Aircraft Workshop. 2017.
5. Williamson M. Air Power the Rise of Electric Air-craft[J]. Engineering & Technology, 2014, 9(10): 77-79..

6. Whurr J, Hart J. A Rolls-Royce Perspective on Concepts and Technologies for Future Green Propulsion Systems[J]. Green Aviation, 2016: 95.
7. ZHAN Jian, ZHANG Zhiming, ZHANG Juannan, et al. Analysis and improvement of rotor dynamics for super high-speed air compressors applied in fuel cell vehicles [J]. Journal of China University of Metrology, 2017(2). DOI: 10.3969/j.issn. 2096-2835.2017.02.006.
8. Cho H W，Ko K J，Choi J Y，et al．Rotor natural frequency in high-speed permanent magnet synchronous motor for turbo-compressor application[J]．IEEE Transactions on Magnetics，2011，47(10)：4258-4261.
9. Lee J G , Lim D K .A Stepwise Optimal Design Applied to an Interior Permanent Magnet Synchronous Motor for Electric Vehicle Traction Applications[J].IEEE Access, 2021.DOI:10.1109/ACCESS.2021.3105119.
10. Credo A , Fabri G , Villani M ,et al.Adopting the Topology Optimization in the Design of High-Speed Synchronous Reluctance Motors for Electric Vehicles[J].IEEE Transactions on Industry Applications, 2020, PP(99):1-1.DOI:10.1109/TIA.2020. 3007366.
11. Tae-Woo Lee; Do-Kwan Hong, Rotor Design, Analysis and Experimental Validation of a High-Speed Permanent Magnet Synchronous Motor for Electric Turbocharger, IEEE Access, vol.10, pp. 21955- 21969, Feb. 2022.
12. WAN G Feng-xiang. Study on design feature and related technology of high speed electrical machines [J]. Journal of Shenyang University of Technology, 2006, 28(3):7.DOI:10.3969/j.issn.1000-1646.2006.03. 005.
13. ZHANG Fengge, DU Guanghui, WANG Tianyu, et al. Rotor Strength Analysis of High-speed Permanent Magnet Under Different Protection Measures [J]. Proceedings of the CSEE, 2013(S1): 8.DOI: CNKI: SUN: ZGDC. 0.2013-S1-031.
14. ZHANG Fengge, DU Guanghui, WANG Tianyu, et al. Rotor containment sleeve study of high-speed PM machine based on multi-physics fields, 2014, 18(6):7.DOI:10.3969/j.issn.1007-449X.2014.06. 003.
15. ZHOU Fengzheng. Investigation of Rotor Eddy-Current Loss in High-Speed PM BLDC Motors. [D],Hangzhou：Zhejiang University, 2008.
16. ZHOU Fengzheng, MENG Qinglin, MENG Zhengzheng, et al. Optimal Design of Rotor Structure and Experimental Study on High Speed PM BLDC Motors [J]. MICROMOTORS, 2019, 52(3): 4.DOI: CNKI: SUN: WDJZ. 0. 2019-03-002.
17. Weili L , Hongbo Q , Xiaochen Z ,et al.Influence of Copper Plating on Electromagnetic and Temperature Fields in a High-Speed Permanent-Magnet Generator[J].IEEE Transactions on Magnetics, 2012, 48(8):2247-2253.DOI:10.1109/TMAG.2012.2190740.
18. Li W , Qiu H , Zhang X ,et al.Analyses on Electromagnetic and Temperature Fields of Superhigh-Speed Permanent-Magnet Generator With Different Sleeve Materials[J].IEEE Transactions on Industrial Electronics, 2013, 61(6):3056-3063.DOI: 10.1109/TIE. 2013.2251740.
19. Li W, Qiu H, Zhang X,et al. Influence of Rotor-Sleeve Electromagnetic Characteristics on High-Speed Permanent-Magnet Generator[J].IEEE Transactions on Industrial Electronics, 2013, 61(6):3030-3037.DOI:10.1109/TIE.2013.2253074.
20. GAO Pengfei, FANG Jiancheng, HAN Bangcheng, et al. Analysis of Rotor Eddy-current Loss in High-speed Permanent Magnet Motors [J]. MICROMOTORS, 2013, 46(5):7.DOI:10.3969/j.issn.1001-6848.2013. 05.002.
21. DONG Jianning, HUANG Yunkai, JIN Long, et al. Review on High Speed Permanent Magnet Machines Including Design and Analysis Technologies [J]. Proceedings of the CSEE, 2014, 34(27):14.DOI:10. 13334/j.0258-8013.pcsee.2014.27.011.
22. GUO Si, GUO Hong, XU Jinquan. Integrated design method of six-phase fault-tolerant permanent magnet in-wheel motor based on multi-physics fields [J]. Journal of Beijing University of Aeronautics and Astronautics, 2019(3):9.DOI:10.13700/j.bh. 1001-5965. 2018.0360.
23. Zhang F , Dai R , Liu G ,et al.Design of HSIPMM based on multi-physics fields[J].IET electric power applications, 2018(8):12.DOI: 10.1049/ iet-epa.2017.0784.
24. HAN Bang-Cheng, XUE Qing-Hao, LIU Xu. Multi-physics analysis and rotor loss optimization of high-speed magnetic suspension PM macine[J].Optics and Precision Engineering, 2017, 025(003):680-688.
25. Kun,Wang,Xin, et al. Multiphysics Global Design and Experiment of the Electric Machine With a Flexible Rotor Supported by Active Magnetic Bearing[J].Mechatronics IEEE/ASME Transactions on, 2019.DOI:10.1109/TMECH.2019.2892392.
26. Jung Y H , Park M R , Kim K O ,et al. Design of High-Speed Multilayer IPMSM Using Ferrite PM for EV Traction Considering Mechanical and Electrical Characteristics[J].IEEE Transactions on Industry Applications, 2020, PP(99):1-1.DOI:10.1109/TIA.2020.3033783.
27. Koronides A , Krasopoulos C , Tsiakos D ,et al. Particular Coupled Electromagnetic, Thermal, Mechanical Design of High-Speed Permanent Magnet Motor[J].IEEE Transactions on Magnetics, 2020, PP(99):1-1.DOI:10.1109/TMAG.2019.2957614.
28. Gu Y , Wang X , Gao P ,et al. Mechanical Parametric Sensitivity Analysis of High-Speed Permanent Magnet Synchronous Machine[J].IEEE Transactions on Applied Superconductivity, 2021, PP(99):1-1.DOI:10.1109/TASC.2021.3094436.

 doi:10.20944/preprints202410.2004.v1

29. Kim J H , Kim D M , Jung Y H ,et al. Design of Ultra-High-Speed Motor for FCEV Air Compressor Considering Mechanical Properties of Rotor Materials[J].IEEE Transactions on Energy Conversion, 2021, (Early Access).DOI:10.1109/TEC.2021. 3062646.
30. Wu S , Sun X , Tong W .Optimization Design of High-speed Interior Permanent Magnet Motor with High Torque Performance Based on Multiple Surrogate Models[J]. CES TEMS, 2022(003):006.DOI:10.30941/CESTEMS.2022.00033.
31. Issah Ibrahim, Rodrigo Silva, David A. Lowther. Application of Surrogate Models to the Multiphysics Sizing of Permanent Magnet Synchronous Motors[J], IEEE Transactions on Magnetics,vol.58, no.9,pp.,sept. 2022.
32. V. R. Joseph, E. Gul, and S. Ba, Maximum projection designs for computer experiments, Biometrika,vol. 102, no. 2, pp. 371–380, Jun. 2015.
33. M. Li, F. Gabriel, M. Alkadri, and D. A. Lowther, Kriging-assisted multi-objective design of permanent magnet motor for position sensorless control, IEEE Trans. Magn.,vol. 52, no. 3, Mar. 2016, Art. no. 7001904.
34. K. Deb, A. Pratap, S. Agarwal, and T. Meyarivan, A fast and elitist multiobjective genetic algorithm: NSGA-II, IEEE Trans. Evol. Comput., vol. 6, no. 2, pp. 182–197, Apr. 2002.